

**Key Points:**

- Dynamic rupture model is consistent with the 2015 Gorkha earthquake slip-pulse duration and propagation speed
- Time-dependent features of the Gorkha earthquake are influenced by rupture geometry and free-surface reflections
- Constraints from near-field GPS recording imply no significant rupture of a shallow ramp

**Supporting Information:**

- Supporting Information S1

**Correspondence to:**

Y. Wang,  
yow004@ucsd.edu

**Citation:**

Wang, Y., Day, S. M., & Denolle, M. A. (2019). Geometric controls on pulse-like rupture in a dynamic model of the 2015 Gorkha earthquake. *Journal of Geophysical Research: Solid Earth*, 124, 1544–1568. <https://doi.org/10.1029/2018JB016602>

Received 23 AUG 2018

Accepted 9 JAN 2019

Accepted article online 13 JAN 2019

Published online 1 FEB 2019

## Geometric Controls on Pulse-Like Rupture in a Dynamic Model of the 2015 Gorkha Earthquake

Yongfei Wang<sup>1,2</sup> , Steven M. Day<sup>1</sup> , and Marine A. Denolle<sup>3</sup> 

<sup>1</sup>Department of Geological Sciences, San Diego State University, San Diego, CA, USA, <sup>2</sup>Institute of Geophysics and Planetary Physics, Scripps Institution of Oceanography, La Jolla, CA, USA, <sup>3</sup>Department of Earth and Planetary Sciences, Harvard University, Cambridge, MA, USA

**Abstract** The 15 April 2015  $M_w$  7.8 Nepal Gorkha earthquake occurred on a shallowly dipping portion of the Main Himalayan Thrust (MHT). Notable features of the event include (1) the dominance of a slip pulse of about 6-s duration that unlocked the lower edge of the MHT and (2) the near-horizontal fault geometry, which, combined with proximity of the free surface, allows surface-reflected phases to break the across-fault symmetries of the seismic wavefield. Our dynamic rupture simulations in an elastoplastic medium yield earthquake parameters comparable to those deduced from kinematic inversions, including seismic moment and rupture velocity. The simulations reproduce pulse-like behavior predicting pulse widths in agreement with those kinematic studies and supporting an interpretation in which the pulse-like time dependence of slip is principally controlled by rupture geometry. This inference is strongly supported by comparison of synthetic ground velocity with the near-field high-rate GPS recording at station KKN4, which shows close agreement in pulse width, amplitude, and pulse shape. That comparison also constrains the updip extent of rupture and disfavors significant coseismic slip on the shallow ramp segment. Over most of the rupture length, the simulated rupture propagates at a near-constant maximum velocity (~90% of the  $S$  wave speed) that is controlled by the antiplane geometry and off-fault plastic yielding. Simulations also reveal the role of reflected seismic waves from the free surface, which may have contributed ~30% elongation of the slip pulse, and show the potential for significant free-surface interaction effects in shallow events of similar geometry.

### 1. Introduction

On 25 April 2015, a devastating earthquake occurred along the convergent boundary between Eurasian and Indo-Australian plates. Its epicenter is about 77 km northwest of Kathmandu, the capital, and most populous city, of Nepal. The active thrust system in this region, which includes the Main Frontal Thrust along the southern edge of the Sub-Himalayan foothills and the Main Himalayan Thrust (hereafter MHT) dipping gently to the north, has hosted several large, damaging earthquakes, for example, earthquakes in 1505 and 1934 with magnitudes greater than 8. This 2015 earthquake was the largest decollement event in the past 80 years. Its hypocentral depth of 15 km and the absence of observed surface rupture, as well as results from inversions of seismic and geodetic data, all indicate that this event ruptured a portion of the MHT, whose dip angle can then be inferred from the low-angle thrust focal mechanism of the event. A number of essential features of this earthquake have been revealed by multiple types of observations. This  $M_w$  7.8 earthquake, with a peak slip of 5–8 m, ruptured ~140 km along the strike direction and ~60 km along the dip direction and propagated unilaterally southeastward at a velocity of ~3.0 km/s. These first-order results have been derived from finite-fault inversions (Avouac et al., 2015; Galetzka et al., 2015; Grandin et al., 2015; Qiu et al., 2016; Wang & Fialko, 2015; Yue et al., 2017) and P-wave teleseismic back-projections (Avouac et al., 2015; Fan & Shearer, 2015; Grandin et al., 2015; Meng et al., 2016; Yagi & Okuwaki, 2015). The event had a pulse-like rupture mode (Galetzka et al., 2015; Yue et al., 2017) with a slip pulse of ~20 km in spatial width and ~6 s in temporal duration (Galetzka et al., 2015). Moreover, depth- and frequency-varying rupture properties (Denolle et al., 2015; Yin et al., 2017; Yue et al., 2017) have been observed, with patterns broadly resembling those seen on subduction megathrusts (Yao et al., 2013).

Fault morphology plays an important role in earthquake rupture—from initiation, to evolution, to eventual termination—by modifying localized stress conditions and thereby impacting rupture extent, near-field ground motion, and aftershock triggering (Andrews, 1994; King et al., 1994; Oglesby & Mai, 2012). There have been extensive studies of the MHT fault geometry, upon which the most destructive earthquakes in

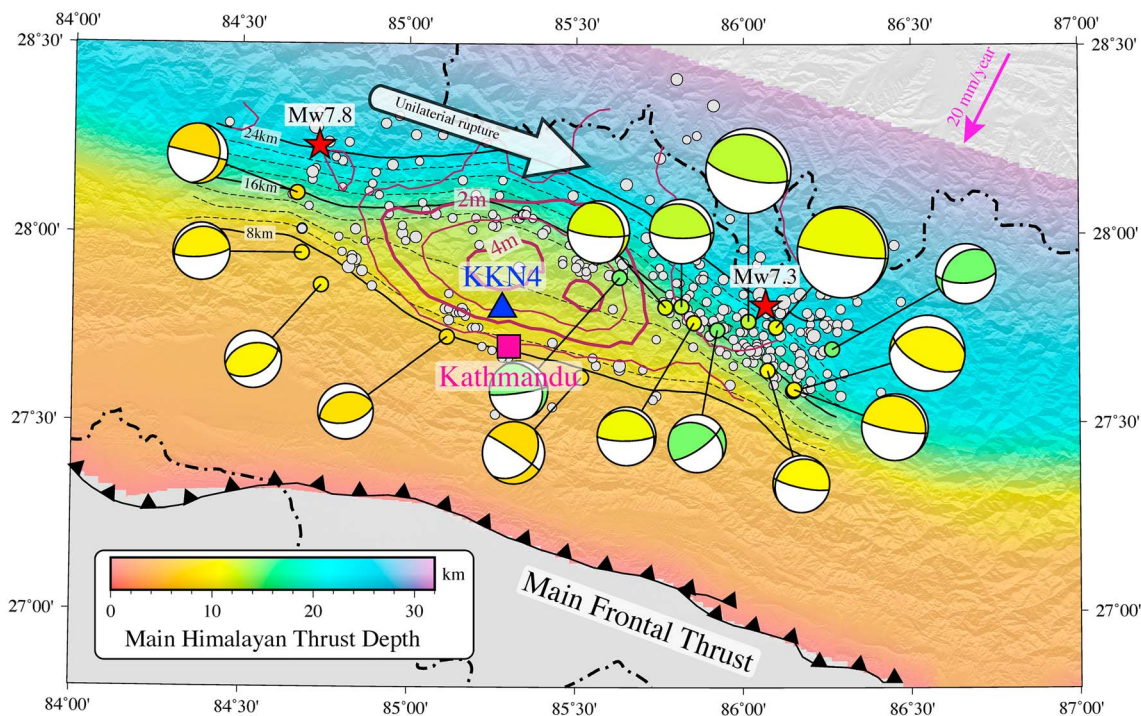


**Figure 1.** Map of the 2015 Gorkha earthquake source region. The fault geometry of the Main Himalayan Thrust (MHT; Hubbard et al., 2016) is illustrated. Wang et al. (2017) indicated that the focal mechanism and locations of relocated large aftershocks (the focal mechanisms are colored by the focal depths) delineate a double-ramp fault geometry that agrees with that in Hubbard et al. (2016; this is indicated by the correlation of the colors between 3-D locations of aftershocks and the Hubbard fault geometry). Black thin solid and dashed lines show the depth contours of adopted MHT geometry. Gray dots denote the location of aftershocks over magnitude 4 within the first 2 months (from the National Seismological Center, Kathmandu, Nepal). The dark red contour lines indicate the coseismic slip profile (Avouac et al., 2015) whose shape is in agreement with the confining edges of this MHT model. The blue triangle and the pink square symbols are the high-rate GPS receiver KKN4 and the capital city Kathmandu, respectively.

the region have occurred. Multiple techniques have been used to explore its geometry in central Nepal, for example, receiver functions (Duputel et al., 2016; Nabelek et al., 2009; Schulte-Pelkum et al., 2005), structural geology (Avouac, 2007; Hubbard et al., 2016; Pearson & DeCelles, 2005), electromagnetic investigations (Lemonnier et al., 1999), microseismicity and focal mechanism studies (Pandey et al., 1995; Wang et al., 2017), geodetic inversion (Elliott et al., 2016), and geodynamical modeling (Cattin & Avouac, 2000; Chamlagain & Hayashi, 2007; Robinson, 2008). Among the shared inferences from these studies are that the MHT serves as a decollement, with a very low dip angle underneath the Lesser Himalaya, steepening along a ramp down to the north beneath the Higher Himalaya and ramping up to the south to merge with the shallower Main Frontal Thrust. While there is broad agreement on the overall geometry, there remains substantial uncertainty in the dip angles and the dimensions of MHT segments. Recently, Hubbard et al. (2016) have incorporated geophysical and geological results (e.g., surface geology, topography, and seismicity) to formulate a detailed fault morphological model. The model contains two ramps truncating the edge of the nearly flat decollement segment along the dip direction and two pinch points confining the dimension of this shallow-dip segment along the strike direction (Figure 1). In this study, we adopt this fault representation of the MHT because this fault geometry is suggested by previous studies to be particularly related to the Gorkha earthquake. For instance, (1) the pattern of coseismic slip for the Gorkha event (Avouac et al., 2015) is in good agreement with expectations from the Hubbard et al. (2016) model, (2) the refined relocations and focal mechanisms determined for 16 aftershocks (Wang et al., 2017, especially their Figure 8), shown in Figure 1, also suggest a double-ramp geometry of the MHT in the region of the mainshock in the form of a concentration of hypocenters delineating a slope change at the northern edge of the main area of coseismic slip, and (3) earthquake cycle modeling based on this fault geometry (Qiu et al., 2016) suggests that the 2015 Gorkha rupture area was limited by fault geometrical features. In the current paper, our aim is to apply dynamic rupture modeling, in conjunction with seismic and geodetic constraints, to examine the physical relationship between the time-dependent aspects of the earthquake (e.g., rupture propagation,

slip-rate function, and near-fault ground motion) and the rupture geometry. The geometrical bounds on rupture in our models were inspired by the underlying model of fault geometry, but the rupture bounds are enforced by imposing fault strength variations that are not explicitly geometrical in origin.

In addition to the fault morphology, the free surface can play a role in the dynamics of rupture. Surface-reflected waves not only interfere with the direct seismic waves from the rupture surface but may also have an effect on the rupture evolution itself (Denolle et al., 2015; Oglesby et al., 1998; Rudnicki & Wu, 1995). It is reasonable to expect this effect to become more prominent in a shallow-thrust scenario such as the Gorkha earthquake. On a shallowly dipping fault, free-surface reflections break the symmetry that pertains for an isolated fault or for a near-surface vertical fault and thereby induce normal stress fluctuations, correspondingly altering fault strength. These fluctuations, and accompanying fluctuations in shear stress, have the potential to interact with rupture processes. Some theoretical studies (e.g., Smith et al., 2005) have found little or no effect on teleseismic peak-to-peak amplitudes from wave-slip interaction associated with surface-reflected phases, but this result may be quite model dependent, and, in any case, it does not imply that near-fault seismic observables are unaffected by those interactions. Additional fault properties such as the presence of a bimaterial interface could further complicate this interaction and lead to enhanced hanging/foot wall effects (Ma & Beroza, 2008). In the case of a normal fault, theory indicates that the free surface can even trigger a shallow nucleation ahead of the main rupture, which could explain the level of high-frequency radiation originating at shallow depth from some normal-faulting events (Nielsen, 1998). In contrast to the models in the foregoing studies, the Gorkha earthquake was an essentially antiplane (Mode III) rupture event on a shallow, and very shallowly dipping, fault surface, a geometry for which free-surface interactions have not been previously modeled (free-surface interactions in 2-D models of the Tohoku earthquake, e.g., Kozdon & Dunham, 2013, and Huang et al., 2014, are for purely Mode II rupture). Therefore, we include in our modeling an exploration of the interaction between free-surface-reflected waves and the rupture process in this event and characterize the extent to which that interaction may affect the character and duration of coseismic slip.

As demonstrated by finite-fault inversions (Galetzka et al., 2015; Yue et al., 2017), the Gorkha rupture propagated unilaterally eastward in a pulse-like slip mode. Pulse-like rupture is one of the two principal end-member models for the space-time dependence of coseismic slip (in contrast to “crack-like”) and has been recognized in many seismological, analytical, computational, and experimental studies (Beeler & Tullis, 1996; Day, 1982; Day et al., 1998; Gabriel et al., 2012; Haskell, 1964; Heaton, 1990; Huang & Ampuero, 2011; Lu et al., 2010; Nielsen & Madariaga, 2003; Noda et al., 2009; Oglesby & Day, 2002; Wang & Day, 2017; Zheng & Rice, 1998). Melgar and Hayes (2017) examined a database of over 150 finite-fault rupture models ( $M_w$  7 to 9) and inferred a pulse-like signature (slip rise times much shorter than the source duration) for the preponderance of them.

A pulse-like rupture mode produces distinct effects (relative to crack-like rupture) on both far-field seismic observations (e.g., a secondary spectral corner, as in Wang and Day, 2017) and near-field ground motions (e.g., compact directivity phases in the fault-normal ground velocity as in Aagaard and Heaton, 2008). Numerous mechanisms have been hypothesized to contribute to pulse-like rupture, including velocity-dependent friction, heterogeneity of fault strength and initial shear stress, and finite downdip rupture dimension (Beeler & Tullis, 1996; Beroza & Mikumo, 1996; Cochard & Madariaga, 1996; Day, 1982; Day et al., 1998; Gabriel et al., 2012; Johnson, 1992; Noda et al., 2009; Oglesby & Day, 2002; Zheng & Rice, 1998). However, it is difficult on the basis of kinematic analysis alone to distinguish these effects on any individual rupture. One complicating factor is uncertainty in the retrieval of the slip-pulse shape, due to factors such as a prior selection of a functional form to represent the source time function, the choice of a single-window or multiwindow inversion method, and ambiguity in defining the end time of the pulse. Some efforts have been made to improve inversions for slip pulses by using insights from dynamic models. Tinti et al. (2005) propose a new source-time function called regularized Yoffe function that is inspired by a self-similar pulse-like solution (Nielsen & Madariaga, 2003) and approximates some generic characteristics of slip calculated in dynamic models of rupture propagation. Apart from these essentially observational limitations, however, kinematic analysis does not address the fundamental uncertainty about how the various hypothesized factors, taken individually, affect pulse shape and duration and, moreover, how those factors may interact.

In this paper, we investigate factors controlling the slip pulse of the 2015 Gorkha earthquake by forward dynamic modeling. We specify a priori the fault geometry and the large-scale stress and frictional preconditions and enforce observational constraints on total seismic moment. The model prediction for rupture velocity compares favorably with observational estimates (as inferred from backprojection studies), and the near-source velocity waveform compares favorably with a very near source high-rate GPS recording that appears to be relatively free of path effects. The results support an interpretation in which slip-pulse duration is principally controlled by the along-dip extent of the rupture. The Gorkha rupture probably interacted with free-surface reflections, which may have added ~30% to the average slip-pulse width. The simulations also support the interpretation that the Gorkha event ruptured, over much of its length, at velocities near the terminal velocity for an antiplane rupture subject to finite yield strength.

## 2. Problem Formulation and Model Setup

We first describe the geographical area for modeling the 2015 Gorkha earthquake and the discretization of the MHT fault surface and surrounding volume. Then we describe our models for the bulk material properties, the hypothesized initial stress state, and constitutive properties on the fault. Finally, we outline the numerical method and computational platform employed.

### 2.1. Computational Domain and Discretization

The model area of interest is enclosed by an orange box in Figure 2a. The dimensions along the  $x$  axis (horizontally directed from the southeast to the northwest),  $y$  axis (horizontally directed from the southwest to northeast), and  $z$  axis (vertically directed downward from the Earth surface) are 200 km, 80 km, and 60 km, respectively. Inside this box, the fault geometry of the MHT is taken from Hubbard et al. (2016). Multiple alternative fault models have been proposed for the source region of the 2015 Gorkha earthquake (e.g., Avouac, 2007; Duputel et al., 2016; Elliott et al., 2016; Lemonnier et al., 1999; Nabelek et al., 2009; Schulte-Pelkum et al., 2005). From among these, we adopted the fault geometry of Hubbard et al. (2016; hereafter referred to simply as the Hubbard model) because of its close relationship with the coseismic slip of the 2015 Gorkha event. The Hubbard model, while based on structural data that are independent of kinematic inversions of the Gorkha earthquake, has a geometry that is consistent with the spatial limits of coseismic rupture. In the Hubbard model there are two ramps along the dip direction, and we will refer to the upper (southern) one as the updip ramp and the lower (northern) one as the downdip ramp. These are separated by an intervening decollement (which we will also refer to as the flat segment) that is terminated along strike, both to the east and to the west, by “pinch points” where the upper and lower ramps merge to yield a single ramp (Figures 1 and 2). A decollement of this form, terminated at narrow junctions, correlates well with the coseismic patch in the Gorkha event. Consequently, the Hubbard model geometry is an appropriate starting point for models of rupture dynamics. The dynamic models can, in turn, help assess the extent to which that geometry controls the time-dependent rupture behavior. We interpolated the triangularized fault surface representation of the Hubbard model (GOCAD data format) onto the structured hexahedral grid employed in our dynamic rupture simulation method. In that grid, the  $x$  and  $y$  axes are equally and orthogonally gridded (100-m intervals), and  $z$  intervals are variable, as required to ensure that both the fault surface and the free surface conform to grid coordinate surfaces. To enhance numerical accuracy in computation of fault-surface tractions, the elements adjacent to the fault on either side have identical shapes and sizes. All remaining  $z$  intervals in the structured, hexahedrally gridded volume are linearly interpolated between the fault and, respectively, the free surface and bottom perfectly matched layer zone (illustrated in Figure 2b). In total, our final mesh is composed of ~960 million hexahedral elements with variable element sizes and shapes.

### 2.2. Bulk Material, Initial Stress State and Fault Constitutive Law

We assume a homogeneous, elastoplastic bulk material in this region. This simplification is appropriate to our objective of investigating the relationship between the complex fault geometry and the dynamics of the rupture. The rupture extent will be constrained by comparing the predicted and observed ground velocity pulse at the KKN4 high-rate GPS station, which, by virtue of its siting on rock directly above the rupture surface of this event, is relatively insensitive to path effects. We assign the elastic properties (given in Table 1) based upon their values at the hypocentral depth, as given by the 1-D model of Avouac et al. (2015). We represent departures from linearly elastic behavior through the Drucker-Prager elastoplastic model

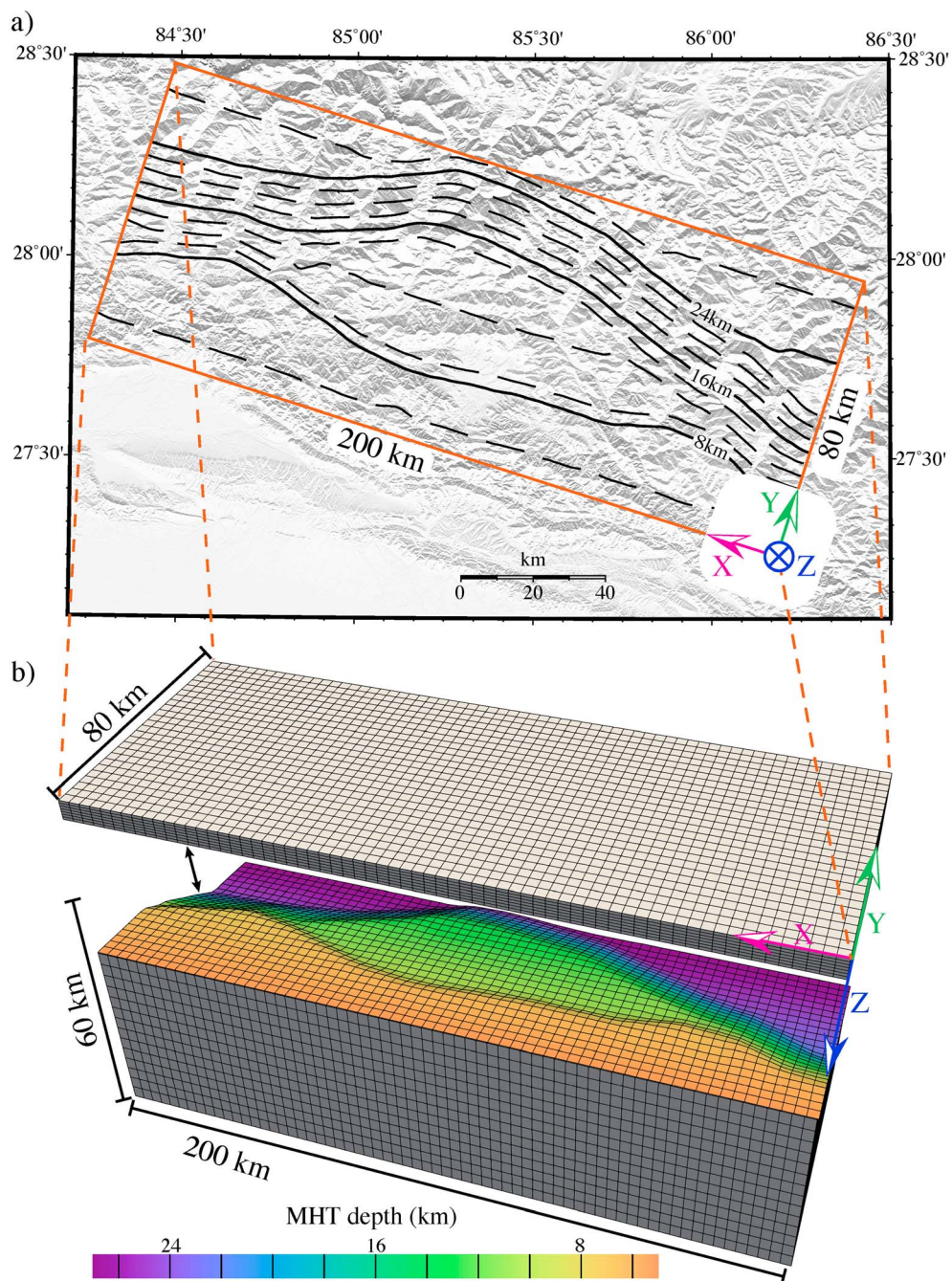


**Figure 2.** Computational domain and geographic map ( $200 \text{ km} \times 80 \text{ km} \times 60 \text{ km}$ ), showing schematically the discretization of this area by an irregular structural hexahedral mesh. The coordinate axes are indicated, with the origin in the southeast. (a) The contour lines show the geometry of the Main Himalayan Thrust (MHT) as given by the Hubbard model. (b) Schematic of the 3-D structured hexahedral mesh is shown, with a cutaway of the fault surface. This schematic mesh is downsampled for illustration purposes.

(Drucker & Prager, 1952), which has been widely used in geomechanics to model pressure-dependent inelastic yielding. It has been long recognized that, if modeled by linear elasticity, the high stresses at the rupture front are likely to exceed the rock strength (Andrews, 1976), and dynamic effects of near-fault plasticity have been the subject of several recent studies (Andrews, 2005; Duan & Day, 2008; Dunham et al., 2011; Gabriel et al., 2013; Ma & Andrews, 2010; Roten et al., 2014, 2017; Shi & Day, 2013). The introduction of plasticity into dynamic models of the Gorkha earthquake reduces the unphysically high

**Table 1**  
*Model Parameter Values*

Parameter	Symbol	Value
Bulk properties		
<i>P</i> wave speed	$\alpha$	5,850 m/s
<i>S</i> wave speed	$\beta$	3,400 m/s
Density	$\rho$	2,640 kg/m <sup>3</sup>
Cohesion	$C$	5 MPa
Internal friction coefficient	$\tan(\phi)$	0.5
Initial stress state		
Initial stress tensor components		
	$\sigma_{xx}$	-142.5 MPa
	$\sigma_{yy}$	-190.0 MPa
	$\sigma_{zz}$	-95.0 MPa
	$\sigma_{yz}^b$	19 MPa
Initial shear stress	$\tau^b$	Variable
Initial normal stress	$\tau^n$	Variable
Frictional properties		
Direct-effect parameter	$a$	Variable
Evolution-effect parameter	$b$	0.014
Reference slip rate	$V_0$	1 $\mu\text{m/s}$
Steady state coefficient at slip rate $V_0$	$f_0$	Variable
Evolution distance of state variable	$L$	Variable
Weakening slip rate	$V_w$	0.1 m/s
Fully weakened friction coefficient	$f_w$	Variable
Initial fault slip rate	$V^{ini}$	$6 \times 10^{-10}$ m/s
Nucleation parameters		
Nucleation radius	$R$	7,500 m
Overstress	$\Delta t^b$	$0.5 \times \tau^b$

Note. All the parameters labeled as “Variable” are illustrated in Figure 3.

shear stresses, and the accompanying high peak slip rates, that develop near the rupture front in purely elastodynamic models. Furthermore, the reduction of the maximum slip rate increases the length of the frictional cohesive zone, which in turn serves to control the contraction of the cohesive zone associated with rupture acceleration toward terminal velocity (Day et al., 2005). Therefore, because numerical solution accuracy requires that the computational grid resolve the minimum cohesive zone (Andrews, 1976; Day et al., 2005), plastic yielding has the ancillary effect in this case (though not in general) of improving numerical accuracy. The Drucker-Prager model formulation is given in Appendix A, and parameter values used in the simulations are listed in Table 1.

The initial stress state is subject to large uncertainties. Even with many simplifying assumptions, geodynamic simulations of frictional sliding on the MHT in Nepal predict complex compressive and tensional stress fields around the fault plane (Chamlagain & Hayashi, 2007), with details sensitive to the details of the fault system geometry. To isolate the first-order dynamic effects associated with the assumed fault geometry (Hubbard model), we simplify the stress state by employing a homogeneous initial stress tensor. This choice neglects, in particular, any increase in effective normal stress with depth. However, in that respect the model is consistent with the suggestion by Rice (1992) that below some depth, the pore pressure follows the lithostatic gradient instead of the hydrostatic trend (and the coseismic patch of the Gorkha event is everywhere below 8 km in depth). The initial stress tensor  $\sigma^0$  is given by

$$\sigma^0 = \begin{pmatrix} \sigma_{xx} & 0 & 0 \\ 0 & \sigma_{yy} & \sigma_{yz} \\ 0 & \sigma_{yz} & \sigma_{zz} \end{pmatrix} \quad (1)$$

where the stress components are listed in Table 1 (the coordinate system is that of Figure 2). In designing this initial stress tensor, we attempt, in the interest of simplicity, to introduce the minimal set of nonzero stress components required to approximate a local stress field consistent with the faulting style and the very low dip angle of the decollement segment. Here, three nonzero normal components of the stress tensor ( $\sigma_{xx}$ ,  $\sigma_{yy}$ , and  $\sigma_{zz}$ ) are first assigned (see Table 1).  $\sigma_{zz}$  is initially set as the effective normal stress of the overburden at a reference depth (initially taken as 8 km, but permitted to vary when we scale to seismic moment, as noted below), assuming hydrostatic pore pressure down to this depth.  $\sigma_{yy}$  is set to  $2\sigma_{zz}$  to mimic a thrust faulting environment (as suggested in Chamlagain and Hayashi, 2007), and  $\sigma_{xx}$  is set to the mean of  $\sigma_{yy}$  and  $\sigma_{zz}$ . Then, we require the ratio between the shear and the normal stress projected onto the fault to approach prior estimates of the apparent frictional properties compatible with the interseismic and long-term deformation. Cattin and Avouac (2000) simulated the long-term and interseismic deformation and infer a low apparent friction coefficient, less than ~0.3, on the decollement segment, which allows thrusting on the MHT with negligible internal deformation of the hanging wall, with a larger value (up to 0.6) on the downdip ramp. Based on those inferences, we rotate the principal stress axes in the  $y$ - $z$  plane by introducing another nonzero stress component  $\sigma_{yz}$ , in order to approximate a shear-to-normal stress ratio of 0.2–0.3 on the decollement segment and ~0.4 on the ramps (these values are stated as approximations because the fault-segment surfaces are not planar, so the resolved stresses have some variation). The higher shear stress on the ramps, relative to the decollement segment, is also seen in earthquake cycle modeling (Michel et al., 2017) that did not impose fault topography but constrained the frictional transitions (velocity strengthening and weakening) based on interseismic observations. The foregoing considerations only fix the ratios of the four independent stress components in equation (1). We then scale these ratios by a constant that is determined by trial and error, such that the seismic moment of the simulation falls within the range of published observational estimates. The resultant shear and normal stresses are illustrated in Figures 3a and 3b.

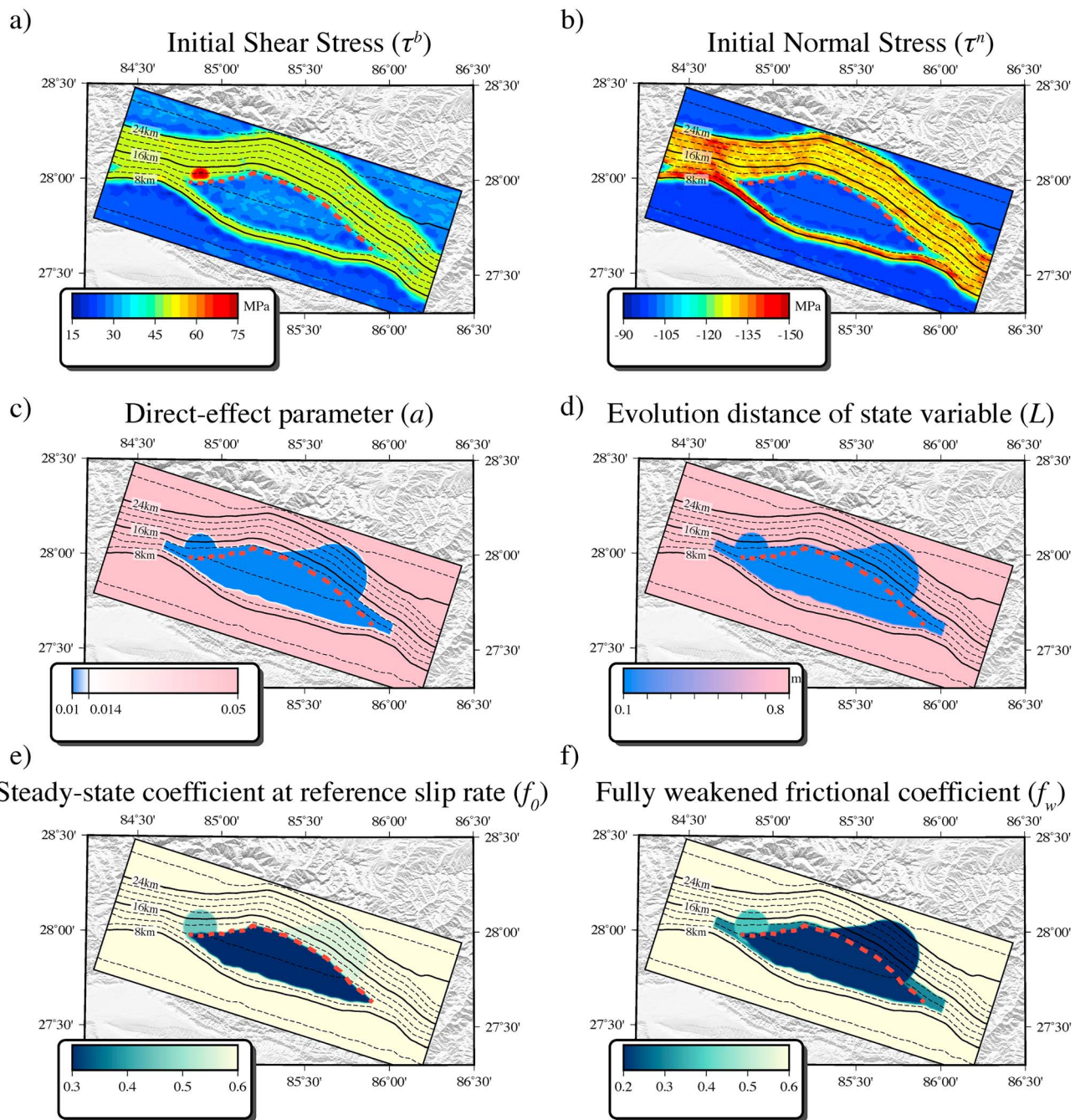


**Figure 3.** Model setup of the projected initial shear and normal stress on fault and four of the frictional parameters (the remaining frictional parameters are constant over the entire fault and are listed in Table 1). The nucleation zone and a lower ramp asperity each show up as intrusive bulges into the lower ramp. The red dashed line shows the lower kink line of the flat decollement. The very narrow white contour band along the downdip edge of the decollement in (c) results from the rapid transition from velocity weakening to velocity strengthening that we have assumed to occur over the depth range between the edge of the decollement and the 14.5-km depth contour.

We introduce an artificial initiation zone on the downdip ramp, near the western pinch point, to initiate the Gorkha earthquake simulation. We move the U.S. Geological Survey hypocenter (within its uncertainty bounds) closer to the western pinch point, because that adjustment reduces the level and spatial extent of the stress perturbation required to initiate a sustained rupture in our model (this is only a computational device to which we attribute no physical significance). Rupture is initiated on the ramp by imposing a Gaussian-shaped shear overstress within a 7,500-m radius of the hypocenter (the red circular overstress

patch in Figure 3a), with peak amplitude 1.5 times the local initial shear stress  $\tau^b$  (details can be found in Equation 11 in Wang and Day, 2017). The overstress in initiation zone results in a maximum ratio of shear to normal stress of 0.6.

The fault friction law is one of rate-dependent dynamic weakening, within a rate and state framework, that has its basis in laboratory experiments (e.g., Dieterich, 1979; Marone, 1998; Ruina, 1983). Here we use the regularized formulation of the friction coefficient proposed by Lapusta et al. (2000), and the steady state friction coefficient is formulated following Dunham et al. (2011), Shi and Day (2013), and Wang and Day (2017). Details of the formulation are given by Equations 6 to 10 in Wang and Day (2017), and the numerical treatment is outlined in Rojas et al. (2009). The evolution-effect parameter  $b$ , the reference slip rate  $V_0$ , and the weakening slip rate  $V_w$  are constant over the fault (see Table 1).

The other frictional parameters are variable and distributed as shown in Figures 3c–3f. We introduce a velocity-weakening portion of the plate interface consisting of the decollement segment, a narrow strip along the top of the downdip ramp down to 14.5-km depth, and a more extensive part of the downdip ramp corresponding to an asperity that appears in many source imaging studies (Avouac et al., 2015; Grandin et al., 2015; Hayes et al., 2015; McNamara et al., 2017; Qiu et al., 2016; Wei et al., 2018; Yue et al., 2017). Apart from that asperity, the lower velocity-weakening boundary follows the 14.5-km depth contour (the white contour band in Figure 3c) and does not coincide exactly with the kink joining the decollement and downdip ramp (dashed red curve in each of Figures 3c–3f). It instead extends a short distance onto the down-dip ramp, and the extra velocity-weakening area near the initiation zone simplifies the nucleation of a sustained rupture (which we just ascribe to the artificiality of our model of event initiation). The velocity-weakening area has direct-effect parameter  $a = 0.01$  ( $b - a = 0.004$ ), state-variable evolution distance  $L = 0.1$  m, and fully velocity-weakened friction coefficient  $f_w = 0.2$  (except on the narrow strip on the downdip ramp, where  $f_w$  is assigned a transitional value of 0.3). The remainder of the downdip ramp, as well as the entire up dip ramp, are velocity strengthening, with  $a = 0.05$ ,  $L = 0.8$  m, and  $f_w = 0.6$  (there is also a very narrow transitional strip between these velocity-strengthening and velocity-weakening regions in which the frictional parameters are smoothly interpolated).

We set the low-velocity friction coefficient  $f_0$  to mirror the pattern of apparent frictional properties proposed by Cattin and Avouac (2000), that is, 0.3 on the decollement and 0.6 on the ramps, except that we reduce it to 0.5 on the asperity portion of the downdip ramp in order to facilitate rupture on that patch. The velocity-weakening value of  $L$  is essentially determined by numerical requirements, in that it is near the minimum value that provides a well-regularized numerical solution, while its high value in the velocity-strengthening zone helps minimize rupture penetration beyond the velocity-weakening region. The value of  $f_w$  is not well constrained, and we chose a value that gives fairly strong dynamic weakening behavior (dynamic friction substantially below final static shear stress); that value trades off against the initial static stress, so the trial-and-error adjustment of the initial stress level (to conform to observational estimates of seismic moment) mentioned earlier is also affected by the choice of  $f_w$ .

The shallow velocity-strengthening zone (i.e., on the up dip ramp) in our model serves as a barrier to rupture on the coseismic timescale (~60 s). The actual geophysical mechanism restricting the upward extent of rupture is not known and may instead be related to insufficient stress accumulation on a fully coupled shallow region (Gualandi et al., 2017; Michel et al., 2017; Stevens & Avouac, 2015; Wang & Fialko, 2018). Our simulated ruptures are not affected by the choice of confinement mechanism (e.g., velocity strengthening versus low stress accumulation).

We solve the 3-D problem of spontaneous rupture propagation within the elastoplastic medium using the Support Operator Rupture Dynamics (Ely et al., 2008, 2009; Shi & Day, 2013). This code implements a generalized finite-difference method that accommodates nonplanar surfaces and nonplanar fault ruptures in a hexahedral mesh. The full methodology has been verified in tens of test problems developed for the Southern California Earthquake Center/U.S. Geological Survey dynamic earthquake rupture code validation exercise (Harris et al., 2009). This application requires ~960 million elements to model the 2015 Gorkha (Nepal) earthquake during a 60-s period, each simulation consuming ~1.3 hr using 16,384 processors on Mira at the Argonne Leadership Computing Facility (Argonne National Laboratory).

### 3. Numerical Simulation Results and Analysis

#### 3.1. Simulated Rupture Propagation and Earthquake Parameters

The simulated dynamic rupture produces, overall, a relatively simple pattern of unilateral eastward rupture but with some complexities related to the fault morphology (Figure 4). The rupture shows a pattern of multiple phases, somewhat similar to that noted in Fan and Shearer (2015). The rupture is first initiated on the downdip ramp close to the western pinch point (Figure 4a). Subsequently, the rupture climbs updip from the ramp onto the decollement segment and is shaped by the pinch-point feature in the west (Figure 4b). This can be associated with Stage 1 in Fan and Shearer (2015). Rupture then evolves into a unilaterally propagating, nearly steady state slip pulse on the decollement segment (Figure 4c). This behavior is common to observation- and simulation-based studies of this event (Galetzka et al., 2015; Michel et al., 2017; Wei et al., 2018; Yue et al., 2017). This phase of rupture corresponds to Stage 2 in Fan and Shearer (2015). The slip-pulse width is roughly 20 km (an estimate of a slip rise time is based upon a threshold slip-rate value for starting and ending of the rupture pulse of 0.1 m/s; alternative estimates are discussed in Text S1), which agrees with the estimate in Galetzka et al. (2015). In dynamic models, slip-pulse width can be affected by multiple factors, including prestress level and dynamic weakening rate (Zheng & Rice, 1998), asperity dimensions (Day et al., 1998), fault-zone low-velocity channels (Huang & Ampuero, 2011), and rupture-surface roughness (Shi & Day, 2013). However, in relatively simple cases, pulse width has a direct relationship to fault width (Day, 1982), so the consistency between observationally inferred and simulated pulse width during rupture of the updip decollement appears to lend support to the view that the rupture is largely confined to that segment. We explore this further in a later section.

The downdip asperity plays a marked role in the next stage of the simulated rupture. As seen in Figures 4d and 4e, the rupture bifurcates, with the major rupture continuing to the southeast and a second branch propagating northeast into the large downdip asperity, with a linear rupture front and shortened pulse width. This phase of the rupture simulation resembles Stage 3 of Fan and Shearer (2015) in location and rupture direction, and the short rise times on the downdip asperity may be related to the depth-dependent radiation inferred by Yue et al. (2017), who find relatively strong high-frequency radiation originating on the downdip asperity. The two branches of rupture are terminated at the eastern pinch point and the northeastern point in the downdip asperity, respectively (Figure 4f). In summary, the simulated dynamics are closely related to the fault geometry and the influence of geometry on fault-resolved shear and normal stress fields, with the shallower (~10-km depth) and deeper (~14-km depth) kinks controlling the rupture pulse width and the two pinch points defining the along-strike extent.

Next, we examine the final static values of coseismic slip and the corresponding changes in shear and normal stress. Recall that the simulation inputs were calibrated to agree with independent seismic moment estimates. The simulation moment is  $6.4 \times 10^{20}$  N·m (corresponding to  $M_w$ 7.8), compared with an observational range of roughly  $6\text{--}9 \times 10^{20}$  N·m ( $M_w$ 7.8–7.9) for the Gorkha earthquake (Avouac et al., 2015; He et al., 2015; Yue et al., 2017).

The coseismic slip in the simulation (Figure 5a) is composed of two slip patches: a major slip on the decollement and a somewhat smaller slip on the asperity on the downdip ramp. The peak slip of 8 m is located on the decollement segment, to the south of the asperity. This peak slip is slightly larger than most observationally inferred peak coseismic slips (5–7 m; Avouac et al., 2015; Galetzka et al., 2015; Grandin et al., 2015; Hayes et al., 2015; Lay et al., 2017; Wang & Fialko, 2015; Wei et al., 2018; Yagi & Okuwaki, 2015; Yue et al., 2017), because our velocity-weakening zone (motivated by the assumed shape and spatial extent of the decollement segment) restricted the rupture area in the simulation, requiring higher slip to conform with seismic moment estimates. This difference may also arise in part from smoothing in the finite-fault inversion. Notably, one slip inversion model that uses a similar fault geometry finds a value of peak slip very close to ours (Qiu et al., 2016). The location of peak slip is along the northern edge of the decollement segment, just south of the downdip asperity (Figure 5a), which is also very similar to the location of the highest slip in the inversion of Qiu et al. (2016). In the simulation, localization of peak slip in that area may be explained by the broadened fault width caused by the concurrent slip on the downdip asperity.

Figures 5b and 5c show the static shear and normal stress changes for the simulated event. In Figure 5b, the pattern of the shear stress change in areas where it is negative (areas of stress drop) is similar to that of the static slip. The region of stress drop is encompassed by positive shear stress change at its margins, where slip

## Fault slip rate snapshots

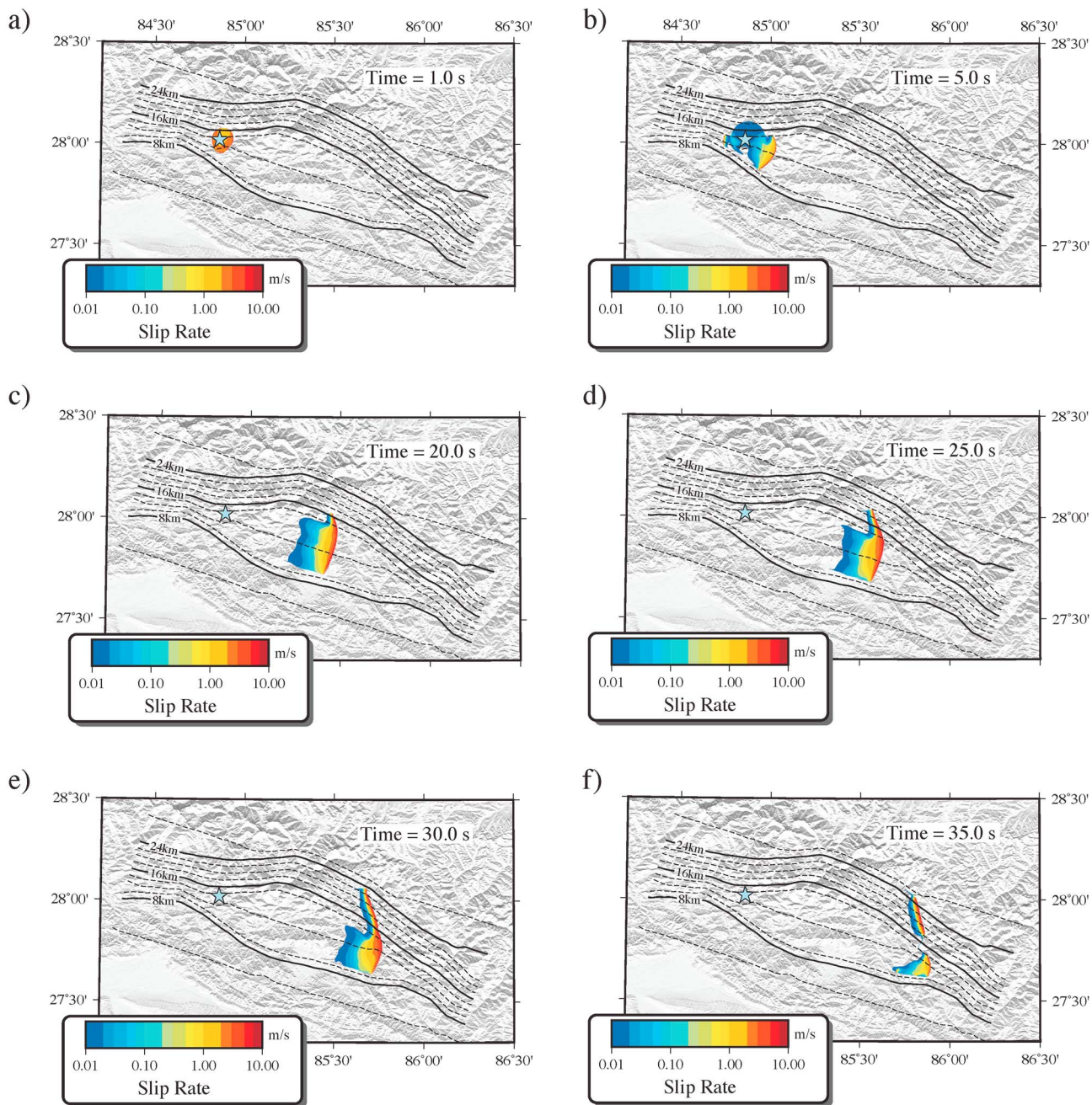


**Figure 4.** Snapshots of the simulated dynamic rupture model of the 2015 Gorkha earthquake at (a) 1, (b) 5, (c) 20, (d) 25, (e) 30, and (f) 35 s. They illustrate the multiple phases of the rupture propagation: the initiation on the lower ramp, the eastward unilateral rupture on the flat segment, the bifurcation of the rupture, and the termination. The light blue star denotes the hypocentral location.

is abruptly suppressed by the transition from velocity weakening to velocity strengthening. The normal stress change in Figure 5c shows some complexities caused by the 3-D fault geometry. The dynamic slip occurring on the kink at the lower edge of the decollement, at ~14-km depth, compresses the fault just below the kink and decompresses the fault above it, with corresponding changes in normal stress (Kase & Day, 2006). This effect is largest along the northeastern edge of the main rupture, where slip is largest (darker blue strip along the northeastern edge). Note also that the aftershocks (denoted by gray circles in Figure 5) have an apparent association with the rupture edge and the fault kink, where large shear and

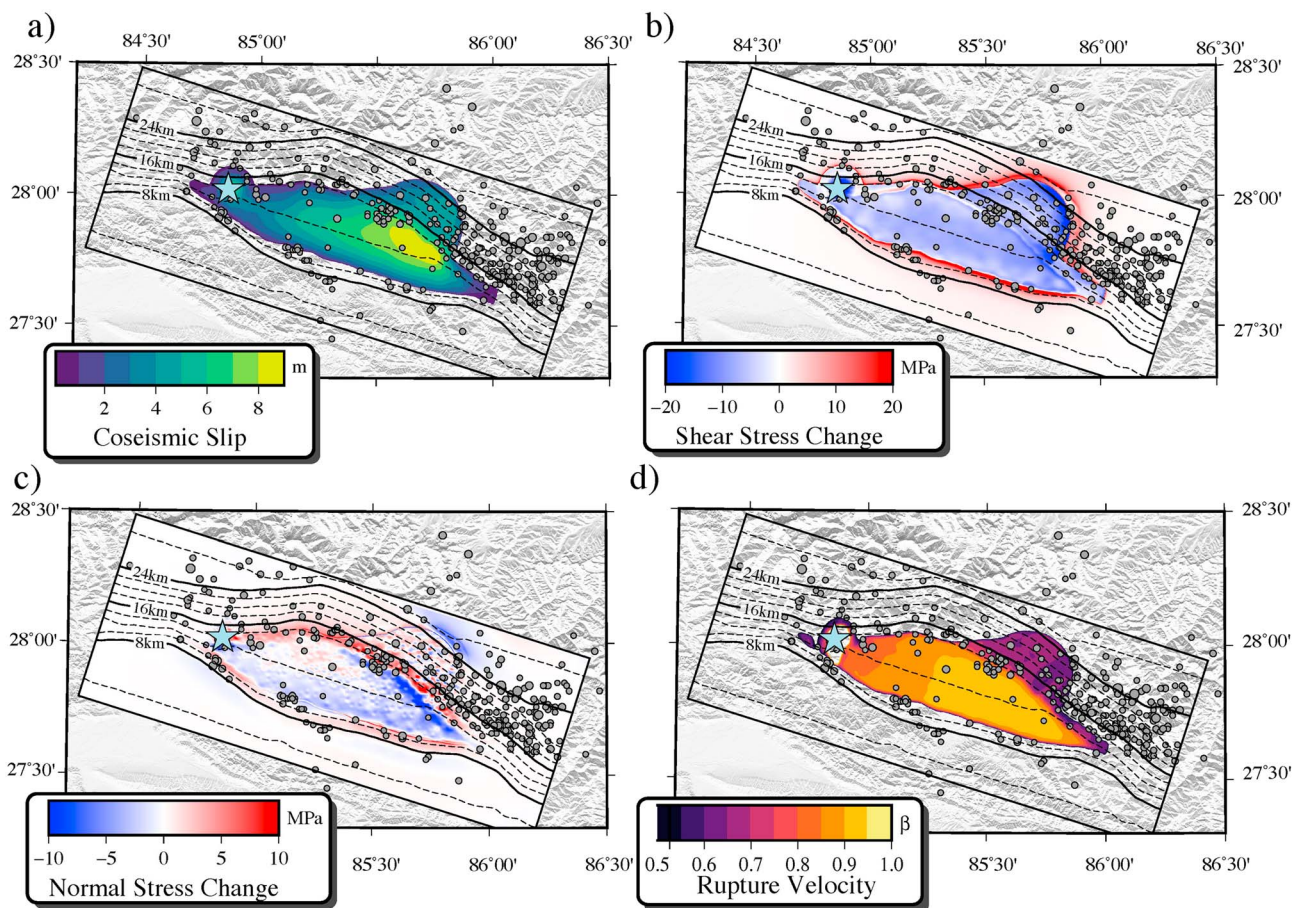


**Figure 5.** Earthquake parameters of simulated dynamic rupture model of the 2015 Gorkha earthquake: (a) coseismic slip, (b) shear stress change, (c) normal stress change, and (d) rupture velocity. Black solid lines enclose the simulated area, and gray dots depict the locations of aftershocks within 4 months of the mainshock. The light blue star denotes the hypocentral location.

normal stress are predicted by the simulation. Das and Henry (2003) note that aftershock clusters are found preferentially at the edges of unbroken barriers and in regions of high spatial gradient of slip. Thus, the aftershock locations are consistent with the decollement bounds used in the simulation. In our simulation, the average stress drop is  $\sim 8$  MPa. Due to the simplicity of our model (e.g., we ignore subsurface sediments, and the geometrical model we adopt places rather strict limits on the potential rupture area), this value may be best viewed as a rough upper bound on the average coseismic stress drop.

Finally, we show the rupture velocity for the simulation in Figure 5d. The spontaneity of rupture results in accelerated rupture, beginning at about 0.7 of the S wave speed as rupture breaks out of the initiation zone and then accelerating to a limiting velocity of about 0.9 of the S wave speed (i.e., about 3.1 km/s). The latter is maintained over most of the rupture extent. The saturation of rupture velocity just below the S speed can be understood from the fact that the Gorkha event approximates antiplane (Mode III) rupture over most of its length. As is well known, an antiplane rupture has a terminal velocity equal to the S wave speed in the elastodynamic case (Andrews, 1976; Kostrov, 1966). Our terminal velocity of  $\sim 0.9$  of the S wave speed is somewhat lower than that, because of the plastic yielding at the rupture front. We confirmed this interpretation by also simulating rupture with the plastic yielding suppressed (Andrews, 2005; Duan & Day, 2008; Gabriel et al., 2013), in which case we find a terminal rupture velocity of 98% of the S wave speed, in close agreement with the elastodynamic theory. The simulation terminal velocity of 3.1 km/s is close to the center of the  $\sim 2.8$ - to 3.3-km/s rupture velocity range inferred by backprojection analysis for the Gorkha earthquake (Avouac et al., 2015; Fan & Shearer, 2015; Lay et al., 2017; Meng et al., 2016; Yagi & Okuwaki, 2015), and the average rupture velocity in the simulation, approximately 2.9 km/s, is also well within that range. The rupture velocity is a quite robust prediction of the simulations, once both geometric bounds of the rupture and an initial

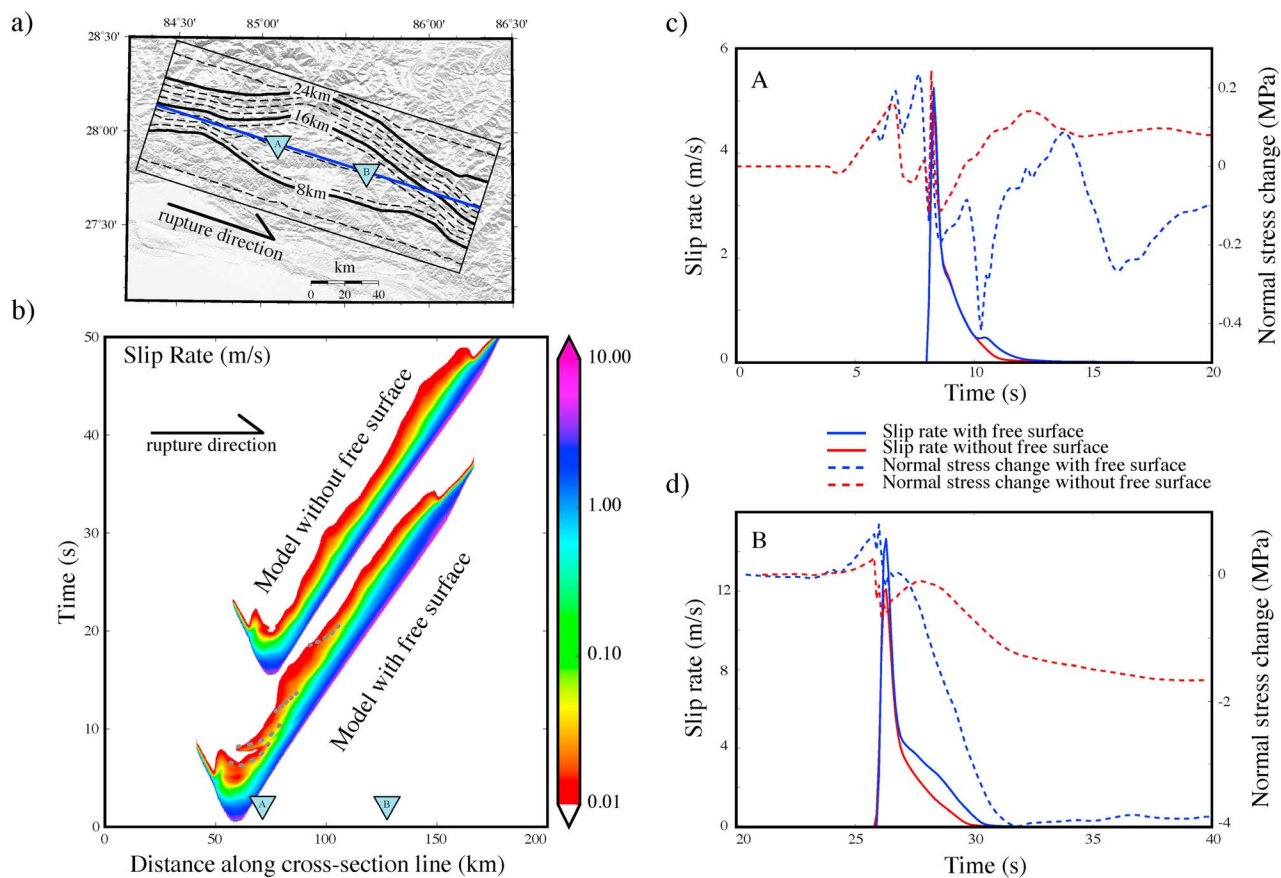


**Figure 6.** Effects of free surface on the rupture evolution. (a) Dark blue straight line shows where the slip-rate and stress histories are extracted. Two sample points on this line, A and B, will highlight the interactions between reflected seismic waves and rupture evolution. (b) The comparison between the model with and without free surface is shown in time-distance plots of the slip rate. The horizontal axis corresponds to the blue cross section from the northwest to the southeast in Figure 6a. (c) The comparison of slip-rate and normal stress histories for models with and without free surface, at point A (closer to the hypocenter). (d) The comparison of slip-rate and normal stress histories for models with and without free surface, at B point (further from the hypocenter).

stress level consistent with the seismic moment are imposed. It should be sensitive to energy dissipation in friction and plastic work near the rupture front (as confirmed by the contrast between elastodynamic and elastoplastic simulations just alluded to), so the agreement with observational estimates provides some degree of validation of our models for those processes.

### 3.2. The Effect of Free Surface on the Dynamic Rupture

In addition to fault nonplanarity, the asymmetry imposed on a nonvertically dipping fault by the presence of the (near-horizontal) free surface can also modify shear and normal stresses, through free-surface-reflected waves (Brune et al., 1993; Oglesby et al., 1998, 2000). Depending upon their strength and timing, these reflections may interact with and modify the rupture. Because the Gorkha earthquake is a large thrust event that is shallow relative to its spatial extent, simulations of the event provide an opportunity to assess the relative importance of such free-surface interactions.

We design a modified simulation that shares all model inputs except that the free surface has been replaced by a perfectly matched layer zone to mimic a whole-space model. In order to compare the rupture evolution for the two cases, we extract slip-rate time histories on an along-strike profile of the fault surface, as indicated in Figure 6a. In that figure, blue triangles denote the surface projections of two points, A and B, that will be used to illustrate the interactions of reflected seismic waves with the rupture. Figure 6b is a time-distance plot comparing slip rates for the Gorkha and modified models, any differences being attributable to rupture interactions with free-surface reflections in the Gorkha model. This time-distance plot shows similar pulse-like rupture in both cases, but several distinctions are evident. First, some bifurcations of the slip-rate function, highlighted by gray dashed lines, appear in the unmodified Gorkha model (i.e., with free surface).

These bifurcations have the appearance of minor ruptures pursuing the main rupture front with higher speed and finally merging with it. But these bifurcations are absent in the model without a free surface, and we can therefore interpret these features as minor ruptures reactivated by reflected seismic waves from the free surface. This interpretation in terms of free-surface reflections is reinforced by the simulation snapshots in Figure S1, where it is clear that the secondary reactivations coincide spatially and temporally with the reflected wave front seen on the cross section of that figure. Second, the model with a free surface has an identifiably longer pulse width. These differences are evident at check points A and B. At check point A (Figure 6c), which is the closer of the two to the hypocenter, the main discrepancy in slip-rate function is that in the half-space model, after the main rupture, a minor subsequent rupture is nucleated. That secondary slip has an amplitude of 0.5 m/s and coincides in time with a sharp reduction of normal stress (blue dashed line). The slip-rate difference is larger at point B (Figure 6d). There, the shape of the slip-rate function for the half-space model deviates markedly from the classic self-similar solution (Kostrov, 1964), whereas the whole-space model resembles the self-similar pulse for several seconds (until it is terminated by effects of rupture finiteness). The slip pulse has been broadened by 1 s or more (depending upon the definition of pulse width that is employed, as discussed in Text S1), and reduction of normal stress is up to 4 MPa. In this geometry, the reflected *S* waves from free surface have particle motion that is vertically upward and horizontally southward at the advancing rupture front (i.e., the free-surface reflection approximately preserves the polarity of the *S* wave). Consequently, the returning *S* waves reduce the normal stress on the fault, lowering frictional resistance, reactivating minor rupture, and increasing slip duration.

To further quantify the effect of the free surface, we calculate the slip rise time (we use “slip rise time” and “pulse duration” interchangeably) throughout the fault. These statistics can shed light on the extent to which free-surface effects similar to those predicted by the simulation might be seismologically resolvable. We retain the definition of rise time used in section 3.1 (and Figure 4), namely, the period between starting and ending threshold slip-rate values of 0.1 m/s. Figure 7 shows rise time spatial distribution across the fault in the Gorkha (half space) and modified (whole space) simulations (Figures 7a and 7b) and a comparison of their histograms (Figure 7c). In each simulation, as seen in Figures 7a and 7b, the patterns for the decollement and downdip asperity segments are distinct from each other (as already noted in the discussion of Figure 4). There are also clear distinctions between the two models. First, as previously shown in Figure 6, rise time on the decollement segment for the half-space model is generally greater than for the whole space. Second, in the whole-space model (Figure 7b), a SE-NW trending pattern of high rise time (south of the downdip asperity) is present, but there is no corresponding coherent feature in the half-space model. The pattern is attributable to the increased fault width on the decollement segment and the corresponding delay of healing. In the half-space model, the rise time is partially controlled by the passage of reflected seismic waves and is less sensitive to healing phases from the rupture edges. The rise time on the downdip asperity remains nearly identical for the two models (Figures 7a and 7b), indicating that the downdip portion of the rupture is insensitivity to the free-surface effects. This insensitivity corresponds with the dependence upon dip angle of the normal-stress perturbation from reflected *S* waves, and, for the dip-angle range in the Hubbard model, the perturbation is stronger for the near-horizontal portion of the fault surface than for the higher-dip portions (e.g., Figure 2 in Oglesby et al., 1998, and Oglesby et al., 2000). This contrast is evident in Figure 7c, where the two peaks (in each model) coincide, respectively, with concentrations of rise time on the decollement and downdip asperity segments. As noted, the rise time on the downdip asperity is only weakly affected by free-surface interaction, while the decollement part shows an average difference of roughly 2 s in rise time. This difference compares with the overall average rise time of approximately 6 s, which is in accord with the observational estimate of Galetzka et al. (2015). A difference of this magnitude may be seismically resolvable, even though it might be difficult or impossible to unambiguously separate a free-surface interaction effect of this level from the many other factors potentially affecting rise time. On the other hand, for an otherwise similar event rupturing to shallower depths, we would expect the free-surface effect on rise time to be even greater, and it could become an essential component in interpreting the rupture kinematics.

### 3.3. The Comparison Between Simulated Near-Field Ground Motions and GPS Signals

Numerous kinematic studies have inferred a pulse-like rupture for the Gorkha earthquake (e.g., Galetzka et al., 2015; Yue et al., 2017), as also shown in the Gorkha dynamic rupture model. The kinematically

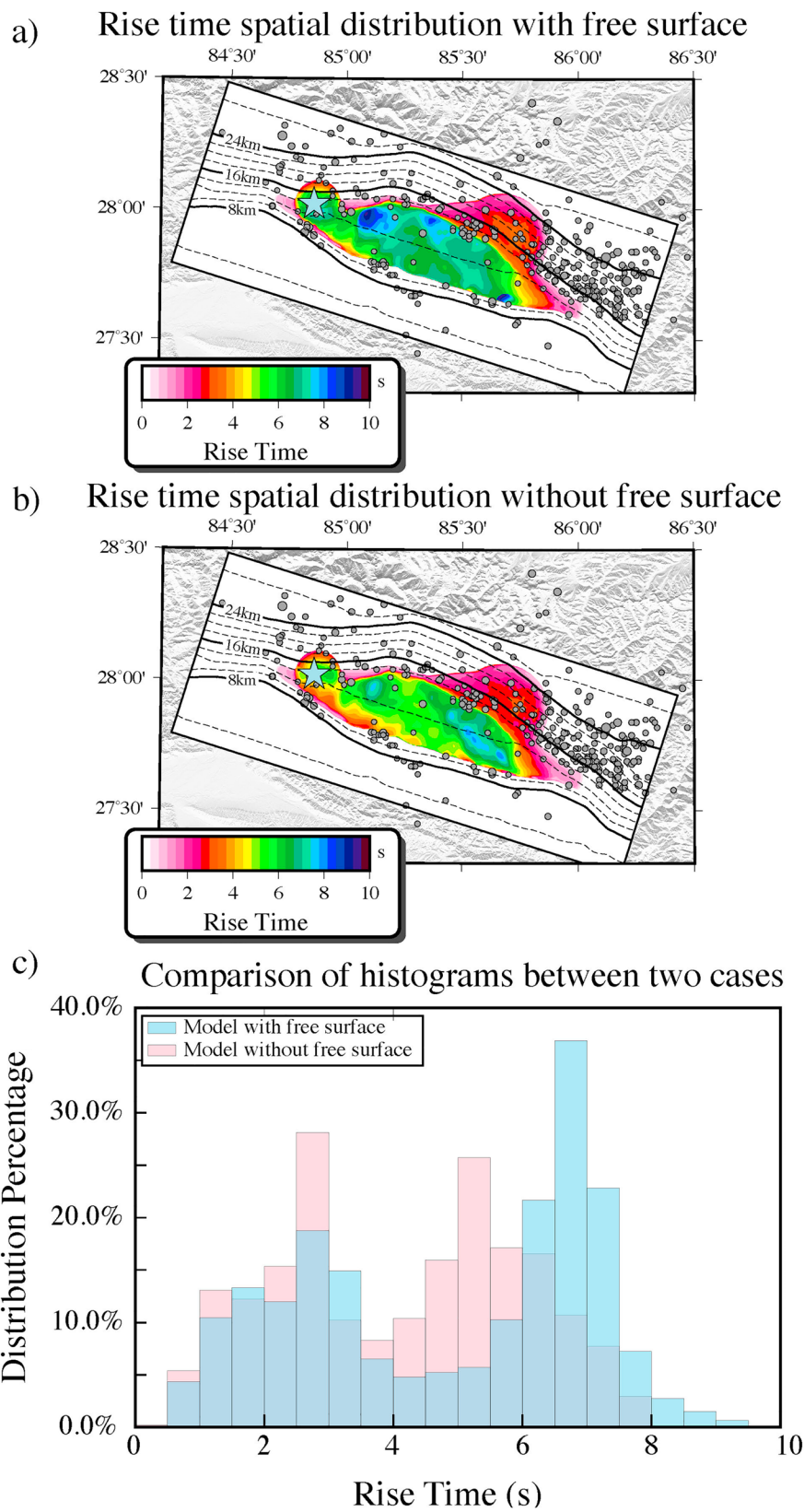


**Figure 7.** Rise time distributions on Main Himalayan Thrust rupture surface and a statistical comparison. (a) Rise time distribution of the half-space model. (b) Rise time distribution of the whole-space model. (c) Rise time histogram for each of the models.

inverted source models (e.g., Galetzka et al., 2015; Wei et al., 2018; Yue et al., 2017) vary somewhat in their estimates of the slip-pulse duration but typically give estimates near 6 s, close to the slip-weighted simulation mean (Figure 7). In simple dynamic models where neither heterogeneities (in, e.g., stress state and near-fault rock stiffness) nor dynamic weakening effects strongly affect rupture duration, pulse duration is controlled principally by the ratio of fault width to rupture velocity, as suggested by dimensional arguments and confirmed by numerical simulations (Day, 1982). If that is a reasonable first approximation for the Gorkha event (as it appears to be for our simulation), then the agreement between simulated and observationally inferred pulse duration may be further evidence supporting the spatial bounds on rupture that we have assumed (and which were, in turn, suggested by the underlying model for fault geometry that we adopted). We further explore that idea in this section by examining the sensitivity of the dynamic source model to downdip and updip geometrical bounds on the rupture. All other model inputs are kept identical to those of our preferred Gorkha model, so that other potential effects on pulse duration, such as the free-surface effects discussed above, are unchanged. Rupture velocity is a simulation result, not an input, but we note that it is not significantly affected by these geometric variations, remaining near the center of the ~2.8- to 3.3-km/s range inferred by backprojection analysis for the Gorkha earthquake (Avouac et al., 2015; Fan & Shearer, 2015; Lay et al., 2017; Meng et al., 2016; Yagi & Okuwaki, 2015).

The 2015 Gorkha earthquake rupture surface on the MHT lies directly beneath a network of high-sample-rate (5 Hz) continuous GPS (cGPS) stations. The pulse-like characteristics of fault slip are reflected in pulse-like ground motion recordings on this close-in network. A distinctly pulse-like motion was recorded right above the rupture at the two cGPS stations, KKN4 and NAST, as well as on an accelerometer at site KATNP (Galetzka et al., 2015), and it is especially clear on the vertical components. The observed ground motion pulse at these stations is closely related to the slip-rate pulses, so these recordings provide constraints on the rupture model. Of these, stations NAST and KATNP are affected by strong oscillations centered at about 3- to 4-s periods and lasting for ~20 s (Galetzka et al., 2015), due to the response of the subsurface sediment within the Kathmandu basin. As our focus is on the inference of source effects, we focus our analysis on the KKN4 station, which is on bedrock and is relatively free of such structure-related oscillations. By comparing the synthetic ground motion at station KKN4 with the observed GPS time history, we assess the factors controlling the simulated slip pulse and obtain some constraints on the geometry of rupture.

Once the initial stress state and frictional parameter values are fixed, the principal remaining factor affecting the simulation results is the location of the frictional transitions (velocity weakening to velocity strengthening) limiting the spatial extent of rupture. We examine the sensitivity of the simulated KKN4 ground motion to rupture geometry by adjusting the updip and downdip limits of the rupture surface (but without altering the geometry of the downdip asperity on the eastern part of the rupture surface). We consider a series of five cases. Case 1 is the preferred Gorkha dynamic rupture model that we have already described, in which we place the upper limit of velocity weakening at the lower edge of the updip ramp (i.e., it precludes rupture on the updip ramp), at a depth of 10.7 km, and the lower limit at 14.5 km. Case 2 is a modification that raises the upper limit of velocity weakening to 9-km depth, permitting a portion of the updip ramp to rupture. Cases 3 and 4 place the upper velocity-weakening limit at 8 and 7 km, respectively. Case 5 places the upper velocity-weakening limit at 10.7 km as in Case 1 but extends the lower limit down to 20 km, permitting rupture on an extended portion of the downdip ramp. These model variants are indicated in Figure 8a, where the blue segment indicates the extent of the velocity-weakening zone and the red segment shows the velocity-strengthening zone.

Figure 8b is a free-surface snapshot illustrating the wing-like shape of the synthetic ground motion pulse (vertical component) that sweeps across the KKN4 station. The KKN4 GPS vertical-component time series (unfiltered) is shown by the gray curve in Figure 8c, along with the corresponding synthetic ground motions for the five cases. More detail about the synthetics can be found in Figure S2. The latter figure also shows that the vertical component has the highest sensitivity to the rupture extent, and we use that component as our primary indicator of model fitness. Our optimal dynamic rupture model, Case 1 (solid dotted curve), shows a very close agreement in shape and amplitude with the recorded KKN4 time series. In Cases 2 through 4 (dashed lines), a very distinct second peak has developed that is absent in the recorded data. This bifurcation of the pulse appears to be related to rupture stepping onto the updip ramp, with the change of dip angle between the flat decollement and shallow ramp complicating the radiation pattern in a manner inconsistent with the recorded waveform. The degradation of the waveform fit for Cases 2–4 suggests that little or no

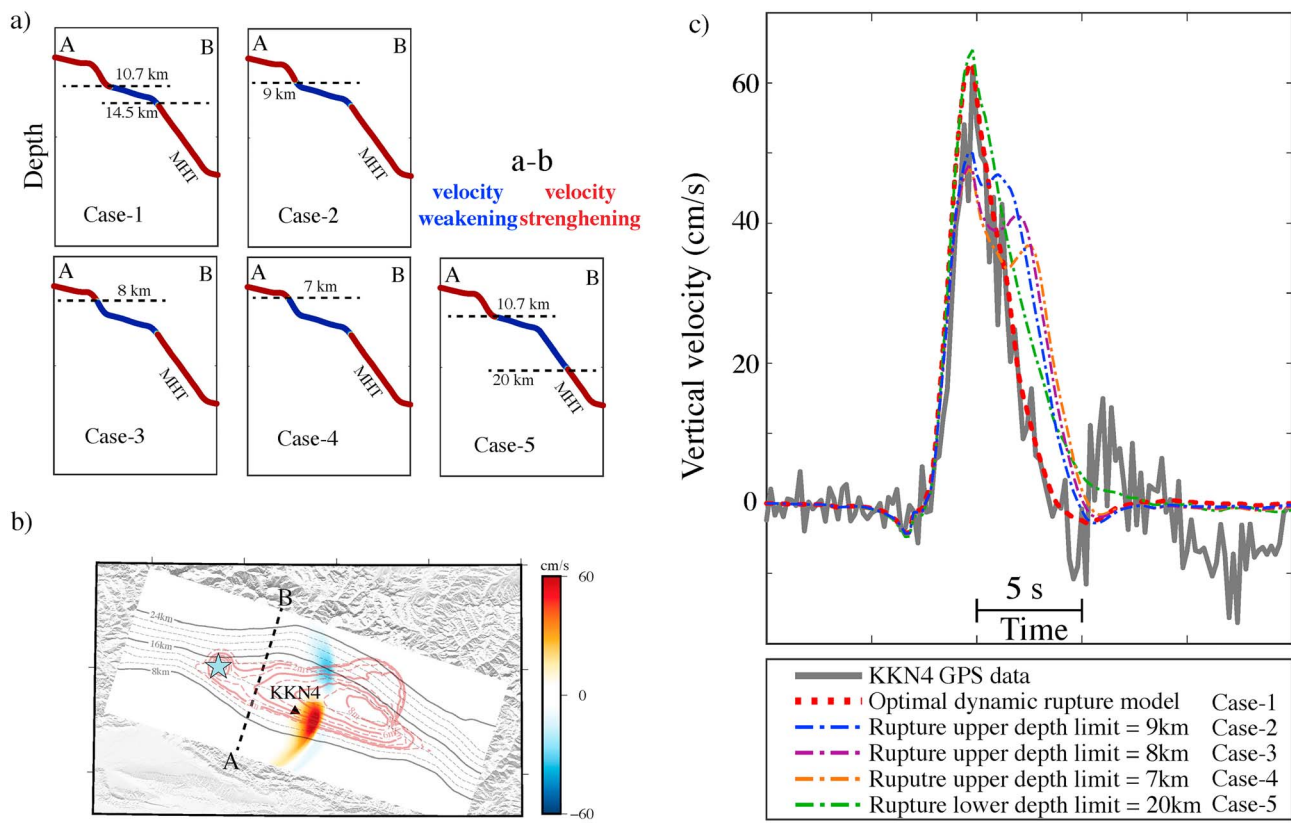


**Figure 8.** (a) The downdip rupture extent (blue and red segments are velocity weakening and strengthening, respectively) along a vertical (cross-section A-B shown in frame (b)) for each of the five simulations used to examine sensitivity to rupture geometry. Case 1 is our optimal model with the upper (10.7 km deep) and lower (14.5 km deep) rupture limits on the middle flat stage. Cases 2–4 are modifications of Case 1 in which the upper limit is raised to 9, 8, and 7 km in depth, respectively. Case 5 is a modification of Case 1 in which the lower limit is moved downward to 20 km. (b) A snapshot of the vertical ground motion at 20 s, along with a dashed line indicating the location of cross-section A-B. The light blue star and black triangle are the locations of the hypocenter and the GPS station (KKN4), respectively. The contours of the depth of the MHT and simulated coseismic slip are plotted by black and brown lines. (c) The simulated (red dotted line) is the optimal dynamic rupture model; the blue, purple, orange, and green dashed lines are from other four alternative models and recorded (gray solid line) vertical ground velocity at the site of KKN4.

coseismic slip occurred on a shallow ramp during the Gorkha event. Adjustments to the lower rupture limit, in comparison, have a more minor effect on pulse shape but make the ground motion pulse wider than the recorded pulse (due to the extended fault width). In summary, the synthetic from our preferred model (Case 1) agrees closely in amplitude, duration, and shape with the recorded pulse (a good agreement in the frequency domain between the observed and synthetic ground velocity is also obtained below the maximum acceptable high-frequency limit beyond which the preevent noise level exceeds observed spectrum containing the velocity pulse; Figure S3), the comparisons favor our original choice of downdip rupture limit, and they strongly disfavor models with significant coseismic rupture of an updip ramp. These constraints on rupture extent, combined with aforementioned constraints from matching seismic moment (further supported by the resultant agreement with rupture velocity estimates), leave a very limited range to vary the average stress drop, which is ~8 MPa in our preferred model.

## 4. Discussion

### 4.1. Rupture Extent on the Fault Surface

As shown in section 3.3, the shape and amplitude of the KKN4 time series favor a rupture that is limited in extent to the flat decollement and a portion of the deeper ramp (i.e., limited to the depth range 10.7 to 14.5 km). The synthetic second peak developed in Cases 2 through 4 strongly disfavors coseismic rupture on the shallower (i.e., southwestern) ramp, at least in the area to the west of the KKN4 station. That inference is further supported by the fact that sources of high-frequency seismic radiation have been imaged in

the area near the lower kink but not near the upper kink where the shallow ramp and the flat decollement intersect (e.g., Avouac et al., 2015; Yin et al., 2017). KKN4 was the only bedrock-based recording sufficiently free of path and site effects for our purposes, and its recorded ground velocity pulse mainly reflects the rupture occurring below and to the west of KKN4. For that reason, there is more uncertainty in the updip rupture extent southeastern of KKN4, where we cannot rule out some rupture of the shallower ramp. Given a sufficiently realistic seismic velocity profile (e.g., for the Kathmandu basin), more near-field recordings (such as KATNP strong ground motion station) and SNDL (high-rate GPS station) might be exploited to infer the rupture extent in more detail. Such an effort might also shed some light on the origin of the long-period secondary pulse in the KKN4 recording that immediately follows the main pulse and is unexplained in our model.

Compared with the fairly sharp results for the updip limit, the down-dip limit of rupture is rather weakly constrained by matching the KKN4 pulse width, but we can provide a rough estimate of sensitivity. As shown in Figure 8c (Case 5), moving the deeper limit from 14.5- to 20-km depth modifies KKN4 pulse width by about 2 s, corresponding (assuming a roughly linear relationship) to about 2.8-km variation in inferred depth extent per 1-s variation in pulse width. The preferred model (Case 1) fits the observed time series within a few tenths of a second, and rejection of models that predict pulse widths that differ from the preferred case by more than, say, 0.5 s would permit the downdip rupture extent to vary from the preferred model by at most 1.4 km in depth, or 3.2 km along dip. Of course, this estimate only considers one source of uncertainty, so it is no more than a lower bound on that uncertainty.

These findings suggest that the extent of the Gorkha earthquake rupture was limited by the geometry of the MHT fault surface, although that geometrical effect in our model was realized indirectly, by adopting a frictional parameterization compatible with fault topography. The along-dip and along-strike extents of the simulated rupture, and its oval-shaped coseismic slip distribution, in addition to being consistent with most published source models (e.g., Avouac et al., 2015; Galetzka et al., 2015; Wei et al., 2018), also closely correlate with the model of a flat decollement bounded by two ramps along the dip and two pinch points along the strike. The result is that only a small portion of the MHT ruptured during this event, unlike the nearby, devastating 1934  $M_w$  8.4 Nepal-Hihiar earthquake that occurred nearby to the east and that ruptured all the way up to the ground surface. Although the updip limit of the Gorkha event coincides with transition from the decollement to upper ramp in the Hubbard model, the actual mechanism stopping the upward progress of the rupture across this transition is not known. A better understanding would improve our assessment of future seismic hazards from the shallow part of the fault. The partial rupture could result from the structural control of the fault geometry, statically (by modifying initial resolved stresses, as assumed in our model setup) and dynamically (by affecting the localized stresses associated with a kink in the rupture path, as occurs at the lower kink; Kase & Day, 2006). In addition, rupture barrier could arise from spatial variations of frictional or stress properties. The hypothesis that rupture was confined due to a frictional transition from velocity weakening to velocity strengthening at the upper edge of rupture does not appear to be supported by postseismic observations (Gualandi et al., 2017; Wang & Fialko, 2018). As an alternative, Michel et al. (2017) propose that ruptures tend to stay confined within a high-prestress zone near the transition from velocity strengthening to velocity weakening at the lower edge of the locked area, generating pulse-like ruptures that propagate along strike. The implications for future earthquakes and ground motion require exploration through rupture simulations informed by a better understanding of the fault segmentation and mechanics, geological structure, seismic velocity structure, seismicity, and long-term crustal deformation.

#### 4.2. Sensitivity of Ground Motion to Slip-Rate Function

Our preferred Gorkha earthquake simulation reproduces the observed near-field ground velocity pulse (at a site where path effects can be neglected) in both amplitude and shape, without any assumptions about the nature of the fault slip. We now consider the significance of that quantitative agreement by examining the sensitivity of the ground motion to the earthquake slip function.

Analytical formulations of a kinematic source typically consider slip onset time (i.e., rupture velocity, taking into account its spatial variations) and three important parameters of the slip-rate function: peak time (the time between onset and peak of the slip rate, which may in turn be dynamically related to a critical slip distance associated with loss of cohesion), rise time (synonymous with pulse duration, the time between onset

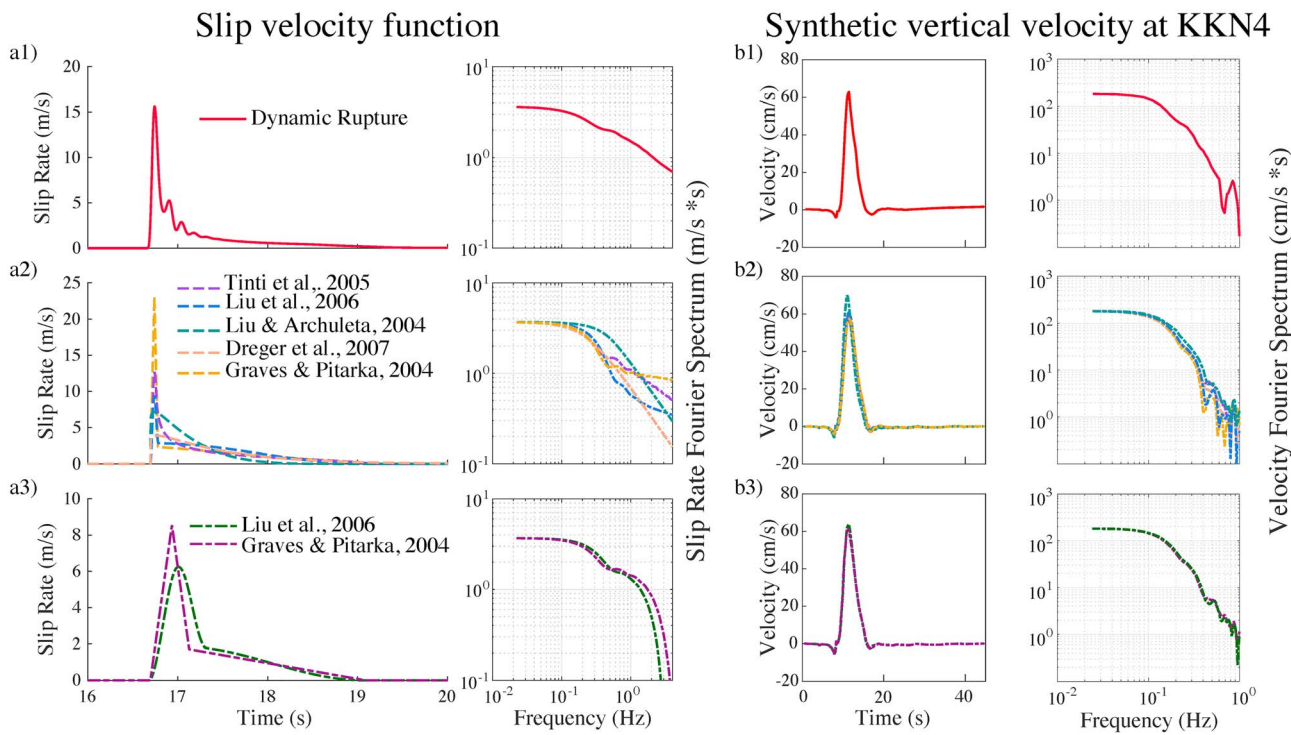


**Figure 9.** (left) Dynamic and equivalent kinematic slip rates, with (right) observed and synthetic vertical ground velocity at KKN4. The dynamic slip rate is from our preferred Gorkha simulation, on the fault surface directly below the point centered between sites A and B in Figure 6a. Equivalent kinematic slip rate is defined in section 4.2. (a1) The slip rate and Fourier amplitude spectrum of the dynamic model. (b1) The synthetic vertical ground velocity for dynamic model, compared with KKN4 record, with the corresponding spectra. (a2) The slip velocities and spectra of equivalent kinematic models (with rise-time, peak-time, and total-slip constraints). (b2) The synthetic vertical ground velocities at KKN4 from the equivalent kinematic models (with rise-time, peak-time, and total-slip constraints). (a3) The slip velocities and spectra of equivalent kinematic models (with rise-time and total-slip constraints only). (b3) The synthetic vertical ground velocities at KKN4 from equivalent kinematic models (rise-time and total-slip constraints only).

and arrest of the slip rate, which may be dynamically related to rupture velocity and rupture extent), and total slip (or time integral of the slip-rate function, which may be related to stress drop and whose spatial integral is proportional to seismic moment). Our strategy here is to (1) extract these parameters (rupture velocity and the three slip-rate parameters) from our dynamic simulation, (2) construct a range of standard kinematic sources that preserve these parameters (which we will call “equivalent kinematic sources”), and then (3) examine the extent to which the equivalent kinematic sources produce ground motion distinguishable from that of the dynamic model (we illustrate this procedure in Figure S6). The representative kinematic sources employed here are those developed in Graves and Pitarka (2004), Liu and Archuleta (2004), Tinti et al. (2005), Liu et al. (2006), and Dreger et al. (2007). In those sources, we fix onset time, peak time, rise time, and total slip to the values extracted from our dynamic simulation, and we follow the authors’ recommendations for other parameters derived from those four, (e.g., for the Liu and Archuleta (2004) source, the  $p$  controlling asymmetry in the slip-rate function is  $p = 5T_p/T_r$  as suggested in Crempien and Archuleta (2014), where  $T_p$  and  $T_r$  are the peak and rise time, respectively). For the analysis, we used the slip rate at a fault point near the center of the rupture area (directly below the point halfway between sites A and B in Figure 6a), which is a good representative of the slip over much of the rupture surface (see, e.g., Figure 6b). The slip-rate functions for the equivalent kinematic sources are displayed in Figure 9, where they are compared with the representative dynamic slip-rate function. As seen in Figure 9a2, the equivalent kinematic slip-rate functions differ in their time-domain shapes and in their spectra, especially at high frequency. Comparing Figures 9a1 and 9a2, it is evident that the equivalent kinematic sources differ from the dynamic simulation at high frequency, despite having the same peak time, rise time, and total slip. This result contrasts with that shown in Figures 9b1–9b3, where we plot the corresponding synthetic ground velocities at KKN4 along with the recorded motion (both synthetic and recorded motion are presented without filtering) in the time and frequency

domain. The equivalent kinematic sources reproduce the recorded motion about as well as does our original dynamic source (once the latter has been used to establish the rupture velocity and slip-rate parameters).

Moreover, we still obtain good agreement even if we relax the constraint that peak time agrees with the dynamic source, and instead apply the prior, empirically defined ratios of peak time over rise time that are recommended by Liu et al. (2006) and Graves and Pitarka (2004) for their respective kinematic sources, for example, 0.13 for Liu et al. (2006) and 0.2 for Graves and Pitarka (2004). In that test, shown in Figure 9a3, we only require the rupture velocity, rise time, and total slip to agree with our dynamic model. The essential point is that the very sharp onsets of the slip-rate functions (as well as the spurious high-frequency oscillations of the dynamically simulated slip rate) are all filtered out by propagation to the KKN4 site, an effect also pointed out by Wei et al. (2018). The result is that, as shown in the last row in Figure 9, at this distance ( $\sim 15$  km), the near-field ground velocity pulse exhibits very weak sensitivity to high-frequency variations of sources, provided we keep the rupture velocity, rise time, and total slip fixed. Of course, in the dynamic Gorkha simulation, these are not free parameters but are all coupled and controlled by the dynamics of the rupture and the initial geometrical constraints.

The fact that ground motion in the near field of a steadily propagating, subshear rupture is a low-pass-filtered image of the slip rate is well known and just reflects the fact that only evanescent waves are excited in that limit. This issue is discussed in detail by Dunham and Archuleta (2005), who also contrast this behavior with the supershear case, and they anticipate precisely the result we noted above (“the slip velocity function will have little effect on the ground motion, so long as the final slip and rise time are preserved”). In their notation, the attenuation factor for wavelength  $\lambda$ , at distance  $y$ , is  $e^{-2\pi\alpha y/\lambda}$ , where  $\alpha = \sqrt{1-V^2/c_s^2}$  ( $V$  is the rupture pulse speed and  $c_s$  is  $S$  wave speed). For 15-km distance (approximately the Gorkha rupture depth), and our inferred rupture velocity of  $\sim 0.9c_s$ , wavelengths of the slip function shorter than about 10 km will be attenuated by a factor of at least  $e^{-4}$  (roughly a factor of 50). Therefore, estimates of rupture parameters such as the critical weakening slip  $D_c$  that require resolution of slip-rate features at a smaller spatial scale than that (e.g., the  $\sim 5$ -m  $D_c$  estimate of Galetzka et al., 2015) are likely to represent, at best, only very weak upper bounds. To illustrate this limitation in the case of  $D_c$ , for example, we note that its estimation relies upon resolution of wavelengths comparable to the dimension  $\Lambda$  of the cohesive zone at the rupture front, which, for Mode III rupture, is of order  $\alpha\mu D_c/\tau$ , where  $\mu$  is the shear modulus and  $\tau$  the stress change across the cohesive zone (see, e.g., Equation 30a of Day et al., 2005). We can insert a reasonable minimum wavelength requirement of  $\sim 2\Lambda$  into the foregoing distance-attenuation factor, obtaining  $e^{-\pi\tau y/(\mu D_c)}$ , and make the rough approximations  $\mu/\tau \approx 4 \times 10^3$  and  $y = 15$  km (approximate nearest distance at which the Gorkha event is recorded). If we assume that resolution is lost when distance attenuation is a factor of  $\sim 10$ , then the minimum resolved  $D_c$  is  $\frac{\pi\tau y}{\mu \ln(0.1)} = 5.1$  m, and a lower  $D_c$  would be undetectable at this station.

#### 4.3. Terminal Rupture Velocity in Elastoplastic Antiplane Rupture

In our simulation, rupture velocity accelerates to 0.9 of the  $S$  wave speed and then maintains approximately that speed over most of the rupture length. This terminal rupture velocity is lower than the terminal rupture velocity (equal to the  $S$  wave speed) that would be approached asymptotically by an elastodynamic antiplane (Mode III) rupture. Moreover, when we suppress plastic yielding in the model, we recover the asymptotic Mode III result to high precision (terminal velocity  $\sim 0.98$  of  $S$  wave speed). Thus, we can unambiguously attribute the simulated rupture velocity to the additional rupture-front dissipation (over and above the modeled frictional losses) supplied by off-fault plastic yielding. Our rupture velocity is an independent (in the sense that it is a modeling result, not an input) and quite robust prediction of the simulations once we impose both the geometric bounds and prestress consistent with the seismic moment and include plastic yielding in the model. The simulated rupture velocity is also consistent with observational estimates (section 3.1) and contributes to a good agreement between the recorded and synthetic ground velocity pulses at KKN4 (section 3.3). The robustness of the simulation prediction for rupture velocity, its sensitivity to off-fault inelastic dissipation, and its apparent agreement with multiple observational inferences appear to support the validity of including a model that permits off-fault dissipation in our dynamic rupture simulation.

The physical rationale for modeling off-fault material as an elastoplastic solid is to accommodate concentrated strain at the rupture front that otherwise would imply very high stresses exceeding rock strength (Andrews, 1976). The consequent energy loss off the fault is known to modify the cohesive zone size and

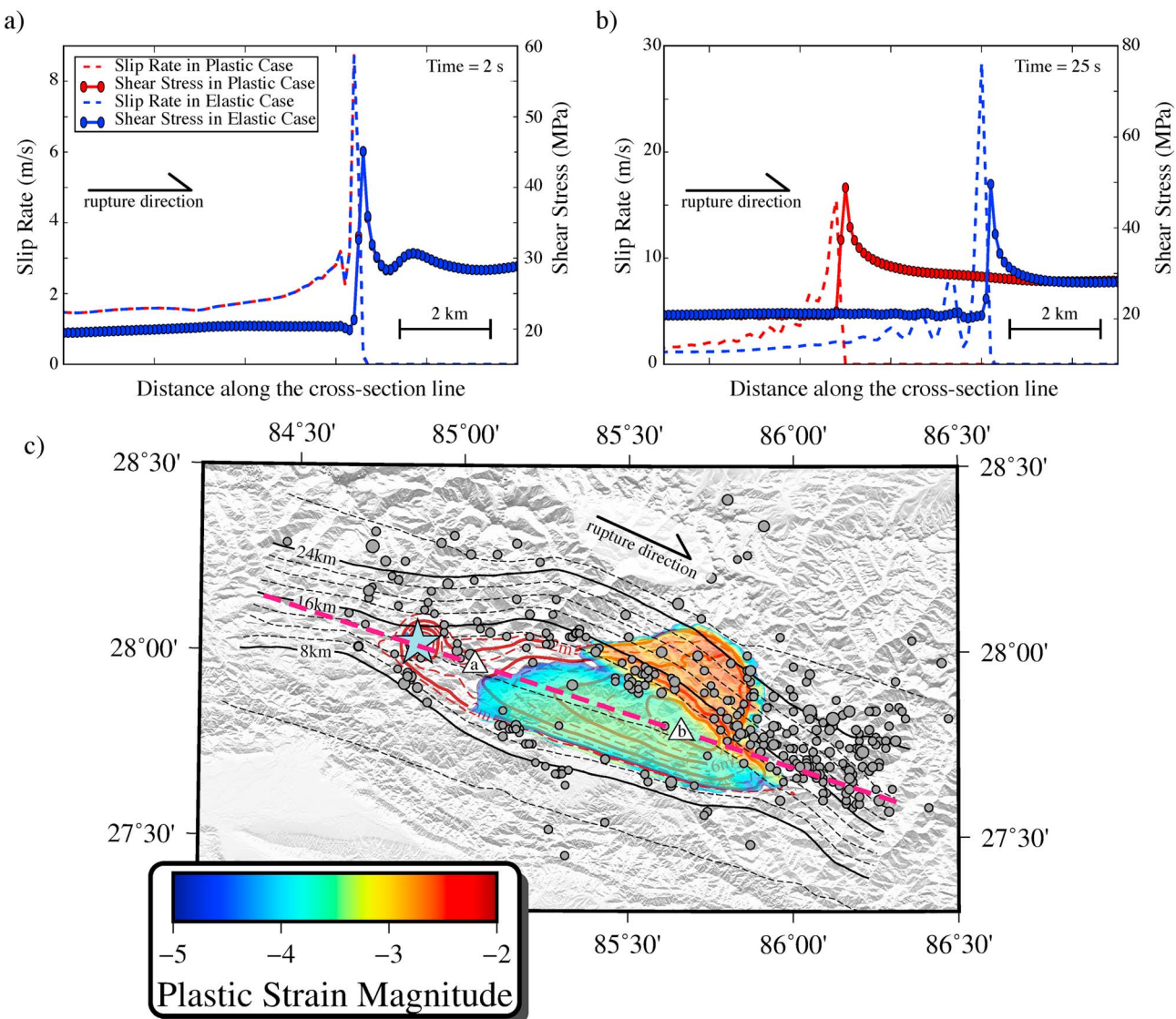


**Figure 10.** Effects of plasticity on the dynamic rupture model. (a) Snapshot, at 2 s, of the slip rate (dashed lines) and shear stress (solid lines with circles) at a local segment (labeled as *a*) of the cross section (pink dashed line from the northwest to the southeast in Figure 10c), for elastic (blue) and elastoplastic (red) cases. (b) Snapshot of slip rate and shear stress at 25 s at a local segment labeled as *b*. (c) The plastic strain magnitude (defined in Appendix A) above the MHT fault surface and synthetic coseismic slip on the Main Himalayan Thrust. Two triangles, labeled *a* and *b*, indicate the locations of stresses and slip rates plotted in Figures 10a and 10b.

rupture velocity (Andrews, 2005). Figure 10 shows the time- and space-dependent nature of these effects in our Gorkha event simulation. As seen in Figure 10a, at an early phase (2 s) in the northwest (labeled as *a*), the difference in shear stress and slip rate between elastic and elastoplastic simulations is negligible, indicating that stresses have remained below the yield surface. But at the later phase (25 s, Figure 10b) in the southeast (labeled as *b*), an appreciable difference is seen. The plastic-case rupture front has been left behind by the elastic-case rupture front, and the plastic-case peak slip rate is capped at about 15 m/s, while the elastic-case slip rate has reached 30 m/s. The rupture velocity for the plastic case has saturated to 90% of the S wave speed (near the center of the range of observational estimates), while that for the elastic case is still accelerating and subsequently saturate at 98% of S wave speed (above the range of observational estimates). Figure 10c shows the accumulated plastic strain magnitude (defined in Appendix A) in the upper material block adjacent to the fault, along with the slip contours for comparison. The plastic deformation generally increases with hypocentral distance, so that it is concentrated in the eastern patch (left side in Figure 10c) where the major slip and downdip asperity are

located. This pattern correlates with the region where most aftershocks are clustered, including the biggest aftershock ( $M_w$  7.3), east of the Gorkha rupture (Figure 1). A possible interpretation of this association is that the inelastic deformation predicted by the simulation is realized as a distribution of near-fault microfractures that promote macroscopic aftershocks.

#### 4.4. Free Surface Effects on Rupture Dynamics

We believe that section 3.2 makes a credible, though speculative, case that there was interaction between the free-surface reflections and the rupture dynamics in the Gorkha earthquake, and we suggest that such interactions would potentially be very significant in a future, shallower event. In the Gorkha simulation, free-surface interaction, on average, extends the slip duration (rise time) by 30% or more, acting preferentially on the low dip-angle segment. In the supplement (Figure S3), we also show that this conclusion is not sensitive to the precise way in which duration is defined. This interaction effect may increase in importance with increased ratio of the spatial slip-pulse width to the rupture depth, because increase of that ratio enables waves from the rupture front to return to the fault surface, as free-surface reflections, before passage of the healing front. Additional analysis can be found in the supporting information (Guatteri et al., 2004; Tinti et al., 2005). Text S1 confirms that the free-surface effect on slip-pulse duration is insensitive to the way we define that duration.

### 5. Conclusions

The Gorkha earthquake was dominated by a slip pulse that ruptured the lower edge of the MHT as it propagated along strike from the northwest to the southeast. Dynamic rupture modeling in an elastoplastic medium clarifies the principal physical factors controlling this slip pulse. The preferred model gives earthquake parameters consistent with published observational estimates (seismic moment  $6.4 \times 10^{20}$  N·m, maximum slip ~8 m, average stress drop ~8 MPa, rupture velocity ~3.1 km/s, average slip-pulse width ~6 s). The agreement for slip-pulse width supports an interpretation that the pulse duration is principally controlled by the narrow dimension of the oval-shaped rupture, and the bounds of that rupture surface appear to reflect geometric features of the underlying fault model that we adopted. An important role for fault geometry is further suggested by comparison of the synthetic near-source velocity waveform with a high-rate GPS recording, which strongly disfavors the extension of significant rupture onto the shallow ramp portion of the model and instead favors confinement of rupture to the flat decollement and a limited, uppermost portion of the deeper ramp, plus a more extended asperity on the northeast portion of that ramp. After its initiation, the rupture front accelerates rapidly to a steady state velocity that is ~90% of the S wave speed, which we interpret as the maximum Mode III rupture velocity consistent with the plastic yielding model (because, when plastic yielding is suppressed in the model, the rupture velocity instead approaches—within 2%—the theoretical maximum for elastodynamic Mode III rupture). In the dynamic simulation, reflected seismic waves from the free surface generate time-dependent normal stress perturbations, prolonging the slip pulse by ~30% (compared with whole-space comparison tests), raising the possibility of potentially significant free surface effects on both rupture propagation and slip in shallow events of similar geometry.

### Appendix A: Formulations of Drucker-Prager Yield Criterion and Inelastic Deformation

The Drucker-Prager plasticity model (Drucker & Prager, 1952) has been widely applied in geomechanics to incorporate inelastic yielding of materials such as rocks and concretes. The Drucker-Prager yield criterion is a smooth approximation to the Mohr-Coulomb yield criterion. The Drucker-Prager yield criterion employed in this study is given by

$$\bar{\tau} \leq \tau^y , \quad (A1)$$

$$\bar{\tau} = \sqrt{\frac{1}{2} s_{ij} s_{ij}} , \quad (A2)$$

$$\tau^y = -\frac{1}{3} \sigma_{kk} \sin\phi + c \cos\phi , \quad (A3)$$

where  $s_{ij}$  is the deviatoric stress component  $s_{ij} = \sigma_{ij} - \frac{1}{3} \sigma_{kk} \delta_{ij}$ ,  $c$  is the cohesion, and  $\phi$  is the internal friction

angle, which together define the yield surface. Elastically calculated increments of  $s_{ij}$  are adjusted at each time step, in equal proportions, as required to bring stress back to the yield surface. During this process, there is no volumetric plastic strain. A measure of accumulated plastic deformation, termed the *plastic strain magnitude*, is defined as

$$\eta = \int \frac{2}{3} d\varepsilon_{ij}^P d\varepsilon_{ij}^P , \quad (A4)$$

$$d\varepsilon_{ij}^P = \frac{ds_{ij}}{2\mu} , \quad (A5)$$

where  $d\varepsilon_{ij}^P$  is the plastic strain increment in each time step, related by (A5) to the deviatoric stress adjustment  $ds_{ij}$ .

## Acknowledgments

The authors thank Shengji Wei, Shuo Ma, Jean-Philippe Avouac, Jiaxun Yin, and Shiying Nie for their helpful discussions and suggestions.

Thoughtful reviews from the Editor, Yehuda Ben-Zion, the Associated Editor, Sylvain Michel, and an anonymous reviewer led to significant improvements in the manuscript. This work was supported partially by The Paul G. Silver Young Scholar Research Enhancement Award at IGPP/UCSD and by NSF award EAR-1135455. The work was also supported by an award of computer time provided by the Innovative and Novel Computational Impact on Theory and Experiment (INCITE) program, through projects GMSeismicSim and SeismicHazard of the Southern California Earthquake Center. This research used resources of the Argonne Leadership Computing Facility, which is a DOE Office of Science User Facility supported under Contract DE-AC02-06CH11357. The postprocessed high-rate GPS records were provided by Shengji Wei. The raw data are available from the UNAVCO website. Most of the data processing and figure generation was carried out using Python, and some map figures were made using GMT (the Generic Mapping Tools, <http://gmt.soest.hawaii.edu/home>). The rupture dynamics code used in this paper is cited in the reference list, and the data for generating figures and tables in this paper are available by contacting the corresponding author at [yow004@ucsd.edu](mailto:yow004@ucsd.edu).

## References

- Aagaard, B. T., & Heaton, T. H. (2008). Constraining fault constitutive behavior with slip and stress heterogeneity. *Journal of Geophysical Research*, 113, B04301. <https://doi.org/10.1029/2006jb004793>
- Andrews, D. J. (1976). Rupture propagation with finite stress in antiplane strain. *Journal of Geophysical Research*, 81(20), 3575–3582. <https://doi.org/10.1029/JB081i020p03575>
- Andrews, D. J. (1994). Fault geometry and earthquake mechanics. *Annals of Geophysics*, 37(6), 1341–1348. <https://doi.org/10.4401/ag-4136>
- Andrews, D. J. (2005). Rupture dynamics with energy loss outside the slip zone. *Journal of Geophysical Research*, 110, B01307. <https://doi.org/10.1029/2004jb003191>
- Avouac, J. P. (2007). Dynamic processes in extensional and compressional settings—Mountain building: From earthquakes to geological deformation. In *Treatise on Geophysics* (pp. 377–439). Amsterdam: Elsevier. <https://doi.org/10.1016/b978-044452748-6.00112-7>
- Avouac, J. P., Meng, L. S., Wei, S. J., Wang, T., & Ampuero, J. P. (2015). Lower edge of locked Main Himalayan Thrust unzipped by the 2015 Gorkha earthquake. *Nature Geoscience*, 8(9), 708–711. <https://doi.org/10.1038/NGEO2518>
- Beeler, N. M., & Tullis, T. E. (1996). Self-slipping slip pulses in dynamic rupture models due to velocity-dependent strength. *Bulletin of the Seismological Society of America*, 86(4), 1130–1148.
- Beroza, G. C., & Mikumo, T. (1996). Short slip duration in dynamic rupture in the presence of heterogeneous fault properties. *Journal of Geophysical Research*, 101(B10), 22,449–22,460. <https://doi.org/10.1029/96JB02291>
- Brune, J. N., Brown, S., & Johnson, P. A. (1993). Rupture mechanism and interface separation in foam rubber models of earthquakes—A possible solution to the heat-flow paradox and the paradox of large overthrusts. *Tectonophysics*, 218(1–3), 59–67. [https://doi.org/10.1016/0040-1951\(93\)90259-M](https://doi.org/10.1016/0040-1951(93)90259-M)
- Cattin, R., & Avouac, J. P. (2000). Modeling mountain building and the seismic cycle in the Himalaya of Nepal. *Journal of Geophysical Research*, 105(B6), 13,389–13,407. <https://doi.org/10.1029/2000jb900032>
- Chamlagain, D., & Hayashi, D. (2007). Neotectonic fault analysis by 2D finite element modeling for studying the Himalayan fold-and-thrust belt in Nepal. *Journal of Asian Earth Sciences*, 29(2–3), 473–489. <https://doi.org/10.1016/j.jseas.2005.10.016>
- Cochard, A., & Madariaga, R. (1996). Complexity of seismicity due to highly rate-dependent friction. *Journal of Geophysical Research*, 101(B11), 25,321–25,336. <https://doi.org/10.1029/96JB02095>
- Crempien, J. G. F., & Archuleta, R. J. (2014). UCSB method for simulation of broadband ground motion from kinematic earthquake sources. *Seismological Research Letters*, 86(1), 61–67. <https://doi.org/10.1785/0220140103>
- Das, S., & Henry, C. (2003). Spatial relation between main earthquake slip and its aftershock distribution. *Reviews of Geophysics*, 41(3), 1013. <https://doi.org/10.1029/2003RG000119>
- Day, S. M. (1982). Three-dimensional finite difference simulation of fault dynamics: Rectangular faults with fixed rupture velocity. *Bulletin of the Seismological Society of America*, 72(3), 705–727.
- Day, S. M., Dalguer, L. A., Lapusta, N., & Liu, Y. (2005). Comparison of finite difference and boundary integral solutions to three-dimensional spontaneous rupture. *Journal of Geophysical Research*, 110(B12), B12307. <https://doi.org/10.1029/2005jb003813>
- Day, S. M., Yu, G., & Wald, D. J. (1998). Dynamic stress changes during earthquake rupture. *Bulletin of the Seismological Society of America*, 88(2), 512–522.
- Denolle, M. A., Fan, W. Y., & Shearer, P. M. (2015). Dynamics of the 2015 M7.8 Nepal earthquake. *Geophysical Research Letters*, 42, 7467–7475. <https://doi.org/10.1002/2015gl065336>
- Dieterich, J. H. (1979). Modeling of rock friction: 1. Experimental results and constitutive equations. *Journal of Geophysical Research*, 84(B5), 2161–2168. <https://doi.org/10.1029/JB084iB05p02161>
- Dreger, D., Tinti, E., & Cirella, A. (2007). Slip velocity parameterization for broadband ground motion simulation, *Seismological Society of America, Annual Meeting*, Hawaii,
- Drucker, D. C., & Prager, W. (1952). Soil mechanics and plastic analysis or limit design. *Quarterly of Applied Mathematics*, 10(2), 157–165. <https://doi.org/10.1090/qam/48291>
- Duan, B., & Day, S. M. (2008). Inelastic strain distribution and seismic radiation from rupture of a fault kink. *Journal of Geophysical Research*, 113, B12311. <https://doi.org/10.1029/2008jb005847>
- Dunham, E. M., & Archuleta, R. J. (2005). Near-source ground motion from steady state dynamic rupture pulses. *Geophysical Research Letters*, 32, L03302. <https://doi.org/10.1029/2004gl021793>
- Dunham, E. M., Belanger, D., Cong, L., & Kozdon, J. E. (2011). Earthquake ruptures with strongly rate-weakening friction and off-fault plasticity, part 1: Planar faults. *Bulletin of the Seismological Society of America*, 101(5), 2296–2307. <https://doi.org/10.1785/0120100075>
- Duputel, Z., Vergne, J., Rivera, L., Wittlinger, G., Farra, V., & Hetenyi, G. (2016). The 2015 Gorkha earthquake: A large event illuminating the Main Himalayan Thrust fault. *Geophysical Research Letters*, 43, 2517–2525. <https://doi.org/10.1002/2016gl068083>
- Elliott, J. R., Jolivet, R., González, P. J., Avouac, J. P., Hollingsworth, J., Searle, M. P., & Stevens, V. L. (2016). Himalayan megathrust geometry and relation to topography revealed by the Gorkha earthquake. *Nature Geoscience*, 9(2), 174–180. <https://doi.org/10.1038/ngeo2623>

- Ely, G. P., Day, S. M., & Minster, J.-B. (2008). A support-operator method for viscoelastic wave modelling in 3-D heterogeneous media. *Geophysical Journal International*, 172(1), 331–344. <https://doi.org/10.1111/j.1365-246X.2007.03633.x>
- Ely, G. P., Day, S. M., & Minster, J.-B. (2009). A support-operator method for 3-D rupture dynamics. *Geophysical Journal International*, 177(3), 1140–1150. <https://doi.org/10.1111/j.1365-246X.2009.04117.x>
- Fan, W. Y., & Shearer, P. M. (2015). Detailed rupture imaging of the 25 April 2015 Nepal earthquake using teleseismic *P* waves. *Geophysical Research Letters*, 42, 5744–5752. <https://doi.org/10.1002/2015gl064587>
- Gabriel, A. A., Ampuero, J. P., Dalguer, L. A., & Mai, P. M. (2012). The transition of dynamic rupture styles in elastic media under velocity-weakening friction. *Journal of Geophysical Research*, 117, B09311. <https://doi.org/10.1029/2012JB009468>
- Gabriel, A. A., Ampuero, J. P., Dalguer, L. A., & Mai, P. M. (2013). Source properties of dynamic rupture pulses with off-fault plasticity. *Journal of Geophysical Research: Solid Earth*, 118, 4117–4126. <https://doi.org/10.1002/jgrb.50213>
- Galetzka, J., Melgar, D., Genrich, J. F., Geng, J., Owen, S., Lindsey, E. O., et al. (2015). Slip pulse and resonance of the Kathmandu basin during the 2015 Gorkha earthquake, Nepal. *Science*, 349(6252), 1091–1095. <https://doi.org/10.1126/science.aac6383>
- Grandin, R., Vallée, M., Satriano, C., Lacassine, R., Klinger, Y., Simoes, M., & Bollinger, L. (2015). Rupture process of the  $M_w = 7.9$  2015 Gorkha earthquake (Nepal): Insights into Himalayan megathrust segmentation. *Geophysical Research Letters*, 42, 8373–8382. <https://doi.org/10.1002/2015gl066044>
- Graves, R., & Pitarka, A. (2004). Broadband time history simulation using a hybrid approach, *Proc. 13th World Conf. Earthq. Eng.*, Vancouver, Canada, paper no. 1098.
- Gualandi, A., Avouac, J. P., Galetzka, J., Genrich, J. F., Blewitt, G., Adhikari, L. B., et al. (2017). Pre- and post-seismic deformation related to the 2015,  $Mw7.8$  Gorkha earthquake, Nepal. *Tectonophysics*, 714–715, 90–106. <https://doi.org/10.1016/j.tecto.2016.06.014>
- Guatteri, M., Mai, P. M., & Beroza, G. C. (2004). A pseudo-dynamic approximation to dynamic rupture models for strong ground motion prediction. *Bulletin of the Seismological Society of America*, 94(6), 2051–2063. <https://doi.org/10.1785/0120040037>
- Harris, R. A., Barall, M., Archuleta, R., Dunham, E., Aagaard, B., Ampuero, J. P., et al. (2009). The SCEC/USGS dynamic earthquake rupture code verification exercise. *Seismological Research Letters*, 80(1), 119–126. <https://doi.org/10.1785/gssrl.80.1.119>
- Haskell, N. A. (1964). Total energy and energy spectral density of elastic wave radiation from propagating faults. *Bulletin of the Seismological Society of America*, 54(6A), 1811–1841.
- Hayes, G. P., Briggs, R. W., Barnhart, W. D., Yeck, W. L., McNamara, D. E., Wald, D. J., et al. (2015). Rapid characterization of the 2015  $Mw 7.8$  Gorkha, Nepal, earthquake sequence and its seismotectonic context. *Seismological Research Letters*, 86(6), 1557–1567. <https://doi.org/10.1785/0220150145>
- He, X. H., Ni, S., Ye, L. L., Lay, T., Liu, Q. X., & Koper, K. D. (2015). Rapid seismological quantification of source parameters of the 25 april 2015 Nepal earthquake. *Seismological Research Letters*, 86(6), 1568–1577. <https://doi.org/10.1785/0220150131>
- Heaton, T. H. (1990). Evidence for and implications of self-healing pulses of slip in earthquake rupture. *Physics of the Earth and Planetary Interiors*, 64(1), 1–20. [https://doi.org/10.1016/0031-9201\(90\)90002-F](https://doi.org/10.1016/0031-9201(90)90002-F)
- Huang, Y. H., & Ampuero, J. P. (2011). Pulse-like ruptures induced by low-velocity fault zones. *Journal of Geophysical Research*, 116, B12307. <https://doi.org/10.1029/2011JB008684>
- Huang, Y. H., Ampuero, J. P., & Kanamori, H. (2014). Slip-weakening models of the 2011 Tohoku-Oki earthquake and constraints on stress drop and fracture energy. *Pure and Applied Geophysics*, 171(10), 2555–2568. <https://doi.org/10.1007/s0024-013-0718-2>
- Hubbard, J., Almeida, R., Foster, A., Sapkota, S. N., Bürgi, P., & Tapponnier, P. (2016). Structural segmentation controlled the 2015  $Mw7.8$  Gorkha earthquake rupture in Nepal. *Geology*, 44(8), 639–642. <https://doi.org/10.1130/g38077.1>
- Johnson, E. (1992). The influence of the lithospheric thickness on bilateral slip. *Geophysical Journal International*, 108(1), 151–160. <https://doi.org/10.1111/j.1365-246X.1992.tb00846.x>
- Kase, Y., & Day, S. M. (2006). Spontaneous rupture processes on a bending fault. *Geophysical Research Letters*, 33, L10302. <https://doi.org/10.1029/2006gl025870>
- King, G. C. P., Stein, R. S., & Lin, J. (1994). Static stress changes and the triggering of earthquakes. *Bulletin of the Seismological Society of America*, 84(3), 935–953.
- Kostrov, B. V. (1964). Selfsimilar problems of propagation of shear cracks. *Journal of Applied Mathematics and Mechanics*, 28(5), 1077–1087. [https://doi.org/10.1016/0021-8928\(64\)90010-3](https://doi.org/10.1016/0021-8928(64)90010-3)
- Kostrov, B. V. (1966). Unsteady propagation of longitudinal shear cracks. *Journal of Applied Mathematics and Mechanics*, 30(6), 1241–1248. [https://doi.org/10.1016/0021-8928\(66\)90087-6](https://doi.org/10.1016/0021-8928(66)90087-6)
- Kozdon, J. E., & Dunham, E. M. (2013). Rupture to the trench: Dynamic rupture simulations of the 11 March 2011 Tohoku earthquake. *Bulletin of the Seismological Society of America*, 103(2b), 1275–1289. <https://doi.org/10.1785/0120120136>
- Lapusta, N., Rice, J. R., Ben-Zion, Y., & Zheng, G. T. (2000). Elastodynamic analysis for slow tectonic loading with spontaneous rupture episodes on faults with rate- and state-dependent friction. *Journal of Geophysical Research*, 105(B10), 23,765–23,789. <https://doi.org/10.1029/2000JB900250>
- Lay, T., Ye, L., Koper, K. D., & Kanamori, H. (2017). Assessment of telesismically-determined source parameters for the April 25, 2015  $Mw 7.9$  Gorkha, Nepal earthquake and the May 12, 2015  $Mw 7.2$  aftershock. *Tectonophysics*, 714–715, 4–20. <https://doi.org/10.1016/j.tecto.2016.05.023>
- Lemonnier, C., Marquis, G., Perrier, F., Avouac, J. P., Chitrakar, G., Kafle, B., et al. (1999). Electrical structure of the Himalaya of Central Nepal: High conductivity around the mid-crustal ramp along the MHT. *Geophysical Research Letters*, 26(21), 3261–3264. <https://doi.org/10.1029/1999gl008363>
- Liu, P. C., & Archuleta, R. J. (2004). A new nonlinear finite fault inversion with three-dimensional Green's functions: Application to the 1989 Loma Prieta, California, earthquake. *Journal of Geophysical Research*, 109, B02318. <https://doi.org/10.1029/2003jb002625>
- Liu, P. C., Archuleta, R. J., & Hartzell, S. H. (2006). Prediction of broadband ground-motion time histories: Hybrid low/high-frequency method with correlated random source parameters. *Bulletin of the Seismological Society of America*, 96(6), 2118–2130. <https://doi.org/10.1785/0120060036>
- Lu, X., Lapusta, N., & Rosakis, A. J. (2010). Pulse-like and crack-like dynamic shear ruptures on frictional interfaces: Experimental evidence, numerical modeling, and implications. *International Journal of Fracture*, 163(1–2), 27–39. <https://doi.org/10.1007/s10704-010-9479-4>
- Ma, S., & Andrews, D. J. (2010). Inelastic off-fault response and three-dimensional dynamics of earthquake rupture on a strike-slip fault. *Journal of Geophysical Research*, 115, B04304. <https://doi.org/10.1029/2009jb006382>
- Ma, S., & Beroza, G. C. (2008). Rupture dynamics on a bimaterial interface for dipping faults. *Bulletin of the Seismological Society of America*, 98(4), 1642–1658. <https://doi.org/10.1785/0120070201>

- Marone, C. (1998). Laboratory-derived friction laws and their application to seismic faulting. *Annual Review of Earth and Planetary Sciences*, 26(1), 643–696. <https://doi.org/10.1146/annurev.earth.26.1.643>
- McNamara, D. E., Yeck, W. L., Barnhart, W. D., Schulte-Pelkum, V., Bergman, E., Adhikari, L. B., et al. (2017). Source modeling of the 2015 Mw 7.8 Nepal (Gorkha) earthquake sequence: Implications for geodynamics and earthquake hazards. *Tectonophysics*, 714–715, 21–30. <https://doi.org/10.1016/j.tecto.2016.08.004>
- Melgar, D., & Hayes, G. P. (2017). Systematic observations of the slip pulse properties of large earthquake ruptures. *Geophysical Research Letters*, 44, 9691–9698. <https://doi.org/10.1002/2017gl074916>
- Meng, L. S., Zhang, A. L., & Yagi, Y. J. (2016). Improving back projection imaging with a novel physics-based aftershock calibration approach: A case study of the 2015 Gorkha earthquake. *Geophysical Research Letters*, 43, 628–636. <https://doi.org/10.1002/2015gl067034>
- Michel, S., Avouac, J., Lapusta, N., & Jiang, J. (2017). Pulse-like partial ruptures and high-frequency radiation at creeping-locked transition during megathrust earthquakes. *Geophysical Research Letters*, 44, 8345–8351. <https://doi.org/10.1002/2017GL074725>
- Nabelek, J., Hetenyi, G., Vergne, J., Sapkota, S., Kafle, B., Jiang, M., et al. (2009). Underplating in the Himalaya-Tibet collision zone revealed by the Hi-CLIMB experiment. *Science*, 325(5946), 1371–1374. <https://doi.org/10.1126/science.1167719>
- Nielsen, S., & Madariaga, R. (2003). On the self-healing fracture mode. *Bulletin of the Seismological Society of America*, 93(6), 2375–2388. <https://doi.org/10.1785/0120020090>
- Nielsen, S. B. (1998). Free surface effects on the propagation of dynamic rupture. *Geophysical Research Letters*, 25(1), 125–128. <https://doi.org/10.1029/97gl03445>
- Noda, H., Dunham, E. M., & Rice, J. R. (2009). Earthquake ruptures with thermal weakening and the operation of major faults at low overall stress levels. *Journal of Geophysical Research*, 114, B07302. <https://doi.org/10.1029/2008jb006143>
- Oglesby, D. D., Archuleta, R. J., & Nielsen, S. B. (1998). Earthquakes on dipping faults: The effects of broken symmetry. *Science*, 280(5366), 1055–1059. <https://doi.org/10.1126/science.280.5366.1055>
- Oglesby, D. D., Archuleta, R. J., & Nielsen, S. B. (2000). The three-dimensional dynamics of dipping faults. *Bulletin of the Seismological Society of America*, 90(3), 616–628. <https://doi.org/10.1785/0119990113>
- Oglesby, D. D., & Day, S. M. (2002). Stochastic fault stress: Implications for fault dynamics and ground motion. *Bulletin of the Seismological Society of America*, 92(8), 3006–3021. <https://doi.org/10.1785/0120010249>
- Oglesby, D. D., & Mai, P. M. (2012). Fault geometry, rupture dynamics and ground motion from potential earthquakes on the North Anatolian Fault under the Sea of Marmara. *Geophysical Journal International*, 188(3), 1071–1087. <https://doi.org/10.1111/j.1365-246X.2011.05289.x>
- Pandey, M. R., Tandukar, R. P., Avouac, J. P., Lave, J., & Massot, J. P. (1995). Interseismic strain accumulation on the Himalayan Crustal Ramp (Nepal). *Geophysical Research Letters*, 22(7), 751–754. <https://doi.org/10.1029/94gl02971>
- Pearson, O. N., & DeCelles, P. G. (2005). Structural geology and regional tectonic significance of the Ramgarh thrust, Himalayan fold-thrust belt of Nepal. *Tectonics*, 24, Tc4008. <https://doi.org/10.1029/2003tc001617>
- Qiu, Q., Hill, E. M., Barbot, S., Hubbard, J., et al. (2016). The mechanism of partial rupture of a locked megathrust: The role of fault morphology. *Geology*, 44(10), 875–878. <https://doi.org/10.1130/G38178.1>
- Rice, J. R. (1992). Fault stress states, pore pressure distributions, and the weakness of the San Andreas Fault. In *51 Fault mechanics and transport properties of rocks—A festschrift in honor of W. F. Brace* (pp. 475–503). San Diego, CA: Academic Press. [https://doi.org/10.1016/s0074-6142\(08\)62835-1](https://doi.org/10.1016/s0074-6142(08)62835-1)
- Robinson, D. M. (2008). Forward modeling the kinematic sequence of the central Himalayan thrust belt, western Nepal. *Geosphere*, 4(5), 785–801. <https://doi.org/10.1130/ges00163.1>
- Rojas, O., Dunham, E. M., Day, S. M., Dalguer, L. A., & Castillo, J. E. (2009). Finite difference modelling of rupture propagation with strong velocity-weakening friction. *Geophysical Journal International*, 179(3), 1831–1858. <https://doi.org/10.1111/j.1365-246X.2009.04387.x>
- Roten, D., Olsen, K. B., & Day, S. M. (2017). Off-fault deformations and shallow slip deficit from dynamic rupture simulations with fault zone plasticity. *Geophysical Research Letters*, 44, 7733–7742. <https://doi.org/10.1002/2017gl074323>
- Roten, D., Olsen, K. B., Day, S. M., Cui, Y., & Fah, D. (2014). Expected seismic shaking in Los Angeles reduced by San Andreas fault zone plasticity. *Geophysical Research Letters*, 41, 2769–2777. <https://doi.org/10.1002/2014gl059411>
- Rudnicki, J. W., & Wu, M. (1995). Mechanics of dip-slip faulting in an elastic half-space. *Journal of Geophysical Research*, 100(B11), 22,173–22,186. <https://doi.org/10.1029/95jb02246>
- Ruina, A. (1983). Slip instability and state variable friction laws. *Journal of Geophysical Research*, 88(B12), 10,359–10,370. <https://doi.org/10.1029/JB088iB12p10359>
- Schulte-Pelkum, V., Monsalve, G., Sheehan, A., Pandey, M. R., Sapkota, S., Bilham, R., & Wu, F. (2005). Imaging the Indian subcontinent beneath the Himalaya. *Nature*, 435(7046), 1222–1225. <https://doi.org/10.1038/nature03678>
- Shi, Z. Q., & Day, S. M. (2013). Rupture dynamics and ground motion from 3-D rough-fault simulations. *Journal of Geophysical Research: Solid Earth*, 118, 1122–1141. <https://doi.org/10.1002/jgrb.50094>
- Smith, D. E., Aagaard, B. T., & Heaton, T. H. (2005). Teleseismic body waves from dynamically rupturing shallow thrust faults: Are they opaque for surface-reflected phases? *Bulletin of the Seismological Society of America*, 95(3), 800–817. <https://doi.org/10.1785/0120030171>
- Stevens, V. L., & Avouac, J. P. (2015). Interseismic coupling on the main Himalayan thrust. *Geophysical Research Letters*, 42, 5828–5837. <https://doi.org/10.1002/2015gl064845>
- Tinti, E., Fukuyama, E., Piatanesi, A., & Cocco, M. (2005). A kinematic source-time function compatible with earthquake dynamics. *Bulletin of the Seismological Society of America*, 95(4), 1211–1223. <https://doi.org/10.1785/0120040177>
- Wang, K., & Fialko, Y. (2015). Slip model of the 2015  $M_w$  7.8 Gorkha (Nepal) earthquake from inversions of ALOS-2 and GPS data. *Geophysical Research Letters*, 42, 7452–7458. <https://doi.org/10.1002/2015gl065201>
- Wang, K., & Fialko, Y. (2018). Observations and modeling of coseismic and postseismic deformation due to the 2015  $M_w$  7.8 Gorkha (Nepal) earthquake. *Journal of Geophysical Research: Solid Earth*, 123, 761–779. <https://doi.org/10.1002/2017jb014620>
- Wang, X., Wei, S. J., & Wu, W. B. (2017). Double-ramp on the Main Himalayan Thrust revealed by broadband waveform modeling of the 2015 Gorkha earthquake sequence. *Earth and Planetary Science Letters*, 473, 83–93. <https://doi.org/10.1016/j.epsl.2017.05.032>
- Wang, Y., & Day, S. M. (2017). Seismic source spectral properties of crack-like and pulse-like modes of dynamic rupture. *Journal of Geophysical Research: Solid Earth*, 122, 6657–6684. <https://doi.org/10.1002/2017jb014454>
- Wei, S. J., Chen, M., Wang, X., Graves, R., Lindsey, E., Wang, T., et al. (2018). The 2015 Gorkha (Nepal) earthquake sequence: I. Source modeling and deterministic 3D ground shaking. *Tectonophysics*, 722(Supplement C), 447–461. <https://doi.org/10.1016/j.tecto.2017.11.024>
- Yagi, Y., & Okuwaki, R. (2015). Integrated seismic source model of the 2015 Gorkha, Nepal, earthquake. *Geophysical Research Letters*, 42, 6229–6235. <https://doi.org/10.1002/2015gl064995>

- Yao, H. J., Shearer, P. M., & Gerstoft, P. (2013). Compressive sensing of frequency-dependent seismic radiation from subduction zone megathrust ruptures. *Proceedings of the National Academy of Sciences of the United States of America*, 110(12), 4512–4517. <https://doi.org/10.1073/pnas.1212790110>
- Yin, J. X., Yao, H. J., Yang, H. F., Liu, J., Qin, W. Z., & Zhang, H. J. (2017). Frequency-dependent rupture process, stress change, and seismogenic mechanism of the 25 April 2015 Nepal Gorkha M-w 7.8 earthquake. *Science China Earth Sciences*, 60(4), 796–808. <https://doi.org/10.1007/s11430-016-9006-0>
- Yue, H., Simons, M., Duputel, Z., Jiang, J., Fielding, E., Liang, C., et al. (2017). Depth varying rupture properties during the 2015  $M_w$  7.8 Gorkha (Nepal) earthquake. *Tectonophysics*, 714–715, 44–54. <https://doi.org/10.1016/j.tecto.2016.07.005>
- Zheng, G., & Rice, J. R. (1998). Conditions under which velocity-weakening friction allows a self-healing versus a cracklike mode of rupture. *Bulletin of the Seismological Society of America*, 88(6), 1466–1483.